POLITECNICO DI TORINO
Repository ISTITUZIONALE

Tuning the activity and selectivity of CuPt/C catalysts for the electrochemical CO2 reduction

Original
Tuning the activity and selectivity of CuPt/C catalysts for the electrochemical CO2 reduction / Gutiérrez-Roa, M., Sebastián, D., Guzmán, H., Zammillo, F., Gallone, M., Hernández, S., Lázaro, M.J., Pérez-Rodríguez, S.. - In: JOURNAL OF CO2 UTILIZATION. - ISSN 2212-9820. - 95:(2025). [10.1016/j.jcou.2025.103084]

Availability:
This version is available at: 11583/2999423 since: 2025-04-22T09:56:54Z

Publisher:
Elsevier

Published
DOI:10.1016/j.jcou.2025.103084

Terms of use:

This article is made available under terms and conditions as specified in the corresponding bibliographic description in the repository

Publisher copyright

(Article begins on next page)

18 November 2026

Journal of CO2 Utilization 95 (2025) 103084

Contents lists available at ScienceDirect

Journal of CO2 Utilization

journal homepage: www.elsevier.com/locate/jcou

Tuning the activity and selectivity of CuPt/C catalysts for the electrochemical CO_2 reduction

M. Gutiérrez-Roa [a], D. Sebastián [a], H. Guzmán [b], F. Zammillo [b], M. Gallone [b], S. Hernández [b], M.J. Lázaro [a], S. Pérez-Rodríguez [a,*]

[a] Instituto de Carboquímica (CSIC), Miguel Luesma Castán 4, Zaragoza 50018, Spain
[b] CREST Group, Department of Applied Science and Technology (DISAT), Politecnico di Torino, Corso Duca degli Abruzzi 24, Turin 10129, Italy

ARTICLE INFO

Keywords:
CO_2 reduction reaction
Bimetallic catalysts
Copper
Platinum
Formate production

ABSTRACT

Copper-based bimetallic catalysts have garnered significant attention for CO_2 electrochemical CO_2 conversion due to their ability to catalytically reduce CO_2 to hydrocarbons and alcohols. Herein, a set of CuPt/C catalysts with different Cu:Pt atomic ratios are successfully synthesised through galvanostatic displacement. The progressive incorporation of platinum on Cu/C nanoparticles significantly impacts the CO_2 electro-reduction performance in a 0.1 M $KHCO_3$ solution. The results revealed that Cu:Pt atomic ratios of 99:1 and 95:5 enhance formate production at mild potentials (-0.6 V vs. RHE) due to an improved water activation compared to monometallic Cu/C and, thus a higher availability of protons (or adsorbed hydrogen, *H) near the active sites. In contrast, lower Cu:Pt ratios or higher overpotentials result in diminished formate production. This behaviour is likely due to the affinity of Pt for the carbon-bound *COOH intermediate, which favors CO formation over formate. These findings demonstrate that Pt incorporation in Cu/C nanoparticles can alter the CO_2 reduction mechanism, providing insights into the design of selective formate-producing catalysts.

1. Introduction

The accumulation of CO_2 in the atmosphere from energy-consuming human activities has precipitated an unprecedented climate crisis in the last century [1]. In this context, the accelerated reduction of CO_2 emissions is critical, along with the development of CO_2 capture, storage, and conversion technologies into other valuable products [2–4].

The electrochemical CO_2 reduction reaction (CO_2RR) to produce fuels and chemicals has recently garnered significant interest as a promising strategy for utilising carbon resources and facilitating the storage of surplus renewable electricity. CO_2RR can yield a wide range of products in aqueous media, including carbon monoxide (CO), hydrocarbons, or alcohols such as methanol or ethanol [5,6]. Formate is also an attractive product due to its various industrial applications. It serves as an intermediate in several chemical and pharmaceutical processes for silage preservation, as an additive in animal feeds, and in textile finishing, among others [7].

The product selectivity of CO_2RR is sensitive to the catalyst structure and composition and the electrolysis conditions (applied potential, electrolyte, temperature, pH, etc.) [8–12]. Copper stands out as the only metal capable of reducing CO_2 to hydrocarbons, aldehydes, and alcohols with substantial faradaic efficiencies [13–18].

Two main CO_2 reduction pathways are generally proposed for copper-based catalysts [19]. In one pathway, CO_2RR proceeds via adsorption of CO (*CO) on the catalyst surface as the first key intermediate, which can then be either desorbed or further reduced to products such as hydrocarbons or alcohols [20–23]. Alternatively, some catalysts favour the formation of a formate intermediate (*OCHO), bonded to the surface by the oxygen atom, which desorbs directly as formate rather than transforming into other products [24,25]. The most common catalysts for enhancing the CO_2-to-formate route are based on In, Sn, or Bi metals, although Cu-based catalysts can also generate such a product [17,26–29]. For instance, Fu et al. developed a $CuBi_3$ catalyst with high faradaic efficiency for formate (98.4 % at −1.1 V vs. RHE) due to spatial and lattice confinement effects [30]. Similarly, Zheng et al. boosted the selective CO_2RR to pure formate with a current density of 1 A cm^{-2} via single-atom Pb alloying of a copper surface [31].

Bimetallic catalysts can significantly alter the catalytic performance of CO_2RR through various mechanisms. Introducing even a slight amount of a second metal may reduce the initial activation energy and

* Corresponding author.
E-mail address: sperez@icb.csic.es (S. Pérez-Rodríguez).

https://doi.org/10.1016/j.jcou.2025.103084
Received 28 November 2024; Received in revised form 27 March 2025; Accepted 13 April 2025
Available online 17 April 2025
2212-9820/© 2025 The Authors. Published by Elsevier Ltd. This is an open access article under the CC BY-NC license (http://creativecommons.org/licenses/by-nc/4.0/).

fine-tune the selectivity due to significant changes in the interaction between the catalyst interface and reaction intermediates [32,33]. Several copper-based bimetallic catalysts have been tested for the active and selective conversion of CO_2 to a specific product [34–38]. Among these metal alloys, platinum has garnered significant attention in the electrocatalysis field due to its capacity for upgrading the generation of H^+, which can promote the activation of CO_2 [39]. Furthermore, Pt can reduce the overpotential for CO_2RR, although it can also promote the competitive hydrogen evolution reaction (HER) [40].

Bimetallic CuPt catalysts have been tested for electrochemical CO_2 conversion with promising results [41–43]. Guo et al. found that CuPt nanocrystals facilitate the CO_2 reduction to CH_4 due to the platinum's affinity for proton production [44]. Furthermore, Zhao et al. optimised the Cu:Pt ratio in CuPt nanocubes (9–10 nm in size) to modulate CO_2RR selectivity, achieving a tuneable range of CO/H_2 ratios depending on the applied potential [45]. To our knowledge, CuPt catalysts primarily promote CH_4 and C_2H_4 production through hydrogenation. Only a previous work reports the selective formate production over Pt/N-doped carbon nanofibers deposited onto a Cu foil as a cathode [42]. However, the authors attributed the unique affinity for formate production to the synergy between the pyridinic-N and Pt sites rather than to a Pt-Cu synergy [42].

In this work, CuPt nanoparticles supported on carbon black (Vulcan XC-72R) with several Cu:Pt ratios are proposed for CO_2RR. Catalysts were prepared by galvanic displacement, resulting in CuPt alloy nanoparticles supported on carbon. Cu:Pt atomic ratios of 99:1 and 95:5 inhibited CO_2RR selectivity to CO compared to the monometallic Cu/C. The tendency for formate production at these catalyst surfaces is explained by the presence of protons (or adsorbed hydrogen) by water activation at mild potentials (less negative than −0.6 V vs. RHE), which promotes CO_2 reduction likely via *OCHO intermediate. However, at more negative potentials or with a higher platinum concentration, the affinity of Pt for the carbon-bound intermediate *COOH results in a decreased selectivity towards formate.

2. Experimental

2.1. Synthesis of the Cu/C and the CuPt/C catalysts

CuPt/C catalysts were synthesised by galvanic displacement following the methodology described in [46]. A pH 3 buffer solution was prepared by dissolving 7.29 g of citric acid ($C_6H_8O_7$, Aldrich, ≥99.5 %) and 3.54 g of sodium citrate ($Na_3C_6H_5O_7$, Aldrich, ≥99 %) in 250 mL of deionised (DI) water. Then, 235.7 mg of $CuSO_4{\cdot}5H_2O$ (Aldrich, 99.995 %) and 240 mg of Vulcan XC-72R (Cabot®) were added to the buffer solution and stirred for 30 min under N_2 atmosphere. After that, Cu^{2+} ions were reduced to Cu^0 by dropwise addition of 50 mL of a 0.26 M aqueous solution of $NaBH_4$ (Aldrich, 99 %). The reduction was kept for 30 minutes under continuous stirring and N_2 purging. On the other hand, a known amount of $H_2PtCl_6{\cdot}6H_2O$ (Aldrich, 8 wt% in H_2O) was dissolved in 50 mL of DI water. This Pt precursor solution was added dropwise to the Cu-containing dispersion under constant stirring and N_2 purging. Pt addition was held for 30 min, affording the galvanic displacement of Cu^0 atoms by Pt^{4+} ions. Finally, the catalysts were filtered, washed with DI water, and dried overnight at 80 °C.

Following this synthesis route, four CuPt/C catalysts were synthesised varying the Cu:Pt ratio: CuPt-99:1/C, CuPt-95:5/C, CuPt-90:10/C and CuPt-75:25/C. A monometallic Cu/C catalyst was also obtained using the same synthesis approach but with no addition of platinum.

2.2. Physicochemical characterisation

The metal content of the catalysts and the Cu:Pt ratio were determined through inductively coupled plasma-optical emission spectrometry (ICP-OES) using a Xpectroblue-EOP-TI FMT26 optical emission spectrometer.

X-ray diffraction (XRD) patterns were obtained using a Bruker AXS D8 Advance diffractometer equipped with CuKα radiation (λ = 0.15406 nm) in a θ-θ configuration. Scans were performed over 2θ values from 10° to 80° with increments of 0.05°. The Pawley method was employed to refine the diffraction data using the TOPAS software. Crystallite sizes were obtained by the Double Voigt approach using peak integral breadth.

Transmission electron microscopy (TEM) images of the catalysts were captured using a Tecnai F30 microscope operating at 300 kV, equipped with a scanning transmission electron microscopy (STEM) module and a high-angle annular dark-field (HAADF) detector. Aberration-corrected HAADF-STEM (AC-HAADF-STEM) images for the CuPt-99:1 catalyst were acquired using an analytical Titan microscope (300 kV). The samples were dispersed in ethanol and deposited onto nickel grids. An energy-dispersive X-ray (EDX) spectroscope combined with the microscopes was employed for qualitative elemental analysis.

An ESCA+ OMICRON optical spectrometer was employed to record X-ray photoelectron spectroscopy (XPS) spectra. The survey scans were acquired at 0.5 eV step, 0.2 s dwell, and 50 eV of pass energy using a Mg anode (hυ = 1253.6 eV) and adjusting anode current and voltage at 15 mA and 15 kV (P = 225 W). High-resolution scans for C 1 s, O 1 s, Cu 2p and Pt 4 f were obtained using a step of 0.1 eV, a dwell of 0.5 s, and a pass energy of 20 eV. XPS data were fitted with the Casa XPS software, applying the sensitivity factors provided by the manufacturer, the Shirley background, and using the C 1 s graphitic peak (284.5 eV) for calibrating the XPS spectra. A 20 %/80 % Gaussian/Lorentzian line shape was used for Cu 2p deconvolution [47], whereas a 70 %/30 % Gaussian/Lorentzian line shape was used to deconvolute Pt 4 f [48]. Pt/(Cu+Pt) ratios were obtained considering peak overlapping of Pt 4 f XPS spectra and Cu 3p region [48].

2.3. Electrochemical characterisation

The electrochemical characterisation of the CuPt/C catalysts was carried out at room temperature in a conventional three-electrode single-compartment cell connected to an Autolab PGSTAT 302 N (Metrohm) potentiostat-galvanostat. Data were acquired and processed using Nova 2.1 software. A high-surface-area carbon rod served as the counter electrode (Gamry), and an Ag/AgCl/KCl (3 M) electrode acted as a reference (0.21 V vs. NHE). The working electrode consisted of a thin layer of the corresponding electrocatalyst ink deposited onto a glassy carbon disk (diameter: 7 mm).

The catalyst inks were prepared by dispersing 2 mg of the powder catalyst in 23 μL of Nafion dispersion (Sigma-Aldrich, 5 wt%) and 644 μL of 1:1 isopropyl alcohol:ultrapure water. The mixture was sonicated for 40 min. The glassy carbon electrode was first polished using alumina particles (Buehler, 0.3 μm) to achieve a mirror-like surface. Then, a known amount of the ink solution was deposited onto the electrode and dried under an inert atmosphere. An active phase (Cu+Pt) loading of 50 μg cm^{-2}, considering the total metal amount determined by ICP, was used for all the electrodes. All the currents in the text are consistently normalised by this Cu+Pt loading.

The working electrode was submerged in a 60 mL aqueous solution of 0.1 M $KHCO_3$ (Aldrich, ≥99.95 %). The electrolyte was saturated with either N_2 (Carburos Métalicos 99.5 %) or CO_2 (Air Liquid, 99.99 %) for 40 minutes, depending on the specific experiment. The pH was determined to be 8.9 when the electrolyte was saturated with N_2 and 6.6 in the presence of CO_2. Unless otherwise specified, potentials in the text are provided versus the reversible hydrogen electrode (RHE) using the following equation in volts (Eq. 1):

$$E_{RHE} = E_{Ag/AgCl} + 0.21 + 0.059\,pH \quad (1)$$

2.4. Product characterisation in an H-type electrochemical cell

The catalysts were characterised in a double-chamber (H-type) electrochemical cell, where the two compartments were separated by a pre-activated anion exchange membrane (AEM) supplied by Fumasep. A 0.1 M $KHCO_3$ solution, continuously bubbled with CO_2 and stirred during the electrochemical tests, was used as the catholyte, while a 0.5 M KOH solution was used as the anolyte. The electrochemical tests were performed with a Biologic VSP-300 multichannel potentiostat.

CO_2 electrolysis experiments were conducted using a three-electrode configuration where a platinum mesh was used as the counter electrode, and an Ag/AgCl/KCl (3 M) electrode was employed as a reference. The working electrodes were prepared by coating a thin layer of the catalysts onto one side of a carbon paper (Sigracet® GDL 39BC). A catalytic ink was first created by ultrasonically dispersing the synthesised catalysts in a mixture containing a Nafion solution (Sigma-Aldrich, 5 wt%) as the binder and ethanol (Sigma-Aldrich, 99 %) as a carrier. This approach ensures that the ink remains fluid, allowing for a uniform spread on the area of interest. The catalyst to Nafion ratio was set at 70:30, while the ethanol/solids mass ratio was 97:3. The dispersion was sonicated for 15 minutes. The ink was applied by airbrushing technique to obtain each electrode with a geometric area of 1 cm^2. The electrodes were then placed on a heating plate at 50°C to ensure complete evaporation of the solvent. The tests were conducted with a catalyst loading of 1 mg cm^{-2}.

For electrochemical measurements, multiple potential cycles were performed in the CO_2-saturated aqueous electrolyte within a potential range of −0.8–0.7 V vs. Ag/AgCl/KCl (3 M) at a scan rate of 20 mV s^{-1} to activate the electrodes. After that, linear sweep voltammetry (LSV) was recorded from 0.0 to −2.0 V vs. Ag/AgCl/KCl (3 M) at a scan rate of 10 mV s^{-1}.

CO_2 electrolysis was conducted by chronoamperometry (CA) at a constant potential for 1.5 hours to assess the electrochemical performance of each catalyst. Afterward, the applied cell potential was ohmic corrected based on the impedance measurement and the current at the selected potential (retrieved from the chronoamperometry). The CO_2 flow rate was regulated at 32 NmL min^{-1} using a mass flow controller (EL-Flow Select, Bronkhorst). The concentrations of gaseous products were measured with an online gas chromatograph (Inficon Micro GC Fusion Gas Analyser) equipped with two channels: a 10 m Rt-Molsieve 5 A column and an 8 m Rt-Q-Bond column, both using thermal conductivity detectors (TCDs). Liquid samples were analysed with a high-performance liquid chromatograph (Shimadzu HPLC) featuring two detectors (RID-10A and PDA 212 nm) and a Rezex ROA Organic Acid column (300 ×7.8 mm). A 5 mM H_2SO_4 aqueous solution was used as the mobile phase. Volatile compounds were further characterised using a gas chromatograph (Perkin Elmer GC, Clarus 580) equipped with a headspace, a Stabilwax-DA column, and a mass spectrometer detector (MSD, SQ8 S). A 3 mL sample of the electrolyte was taken before and after the electrochemical protocol to detect liquid products using HPLC and GC-MSD.

The Faradaic efficiency (FE) for each product was calculated using the Eq. 2:

$$FE(\%) = \frac{z \bullet n \bullet F}{C} \bullet 100 \quad (2)$$

where z represents the number of electrons exchanged at the cathode surface, n is the outlet molar flow rate of each product, F is the Faraday constant (96,400 C mol^{-1}), and C is the total charge obtained from integrating the current during the CA. The selectivity to a specific CO_2RR product was defined as the ratio of the moles of the product to the moles of CO_2 converted, accounting for the stoichiometry of the reaction for each product. All instruments used to detect and quantify CO_2 reduction products were calibrated beforehand.

2.5. Stability tests

The stability of the best-performing electrodes was evaluated by chronoamperometric responses at −0.60 V vs. RHE for 22 h in a CO_2 saturated aqueous solution of 0.1 M $KHCO_3$ with constant carbon dioxide bubbling. A conventional 3-electrode single-compartment electrochemical cell was used for these measurements with a high-surface-area carbon rod as a counter electrode, and an Ag/AgCl/KCl (3 M) electrode as a reference. The working electrodes were prepared by coating a thin layer of the catalysts onto one side of a carbon paper, as described in Section 2.3.

3. Results and discussion

3.1. Physicochemical characterisation of CuPt/C and Cu/C electrocatalysts

The metal loading of the catalysts and the Cu:Pt atomic ratio were determined by ICP-OES (Table 1). The monometallic Cu/C electrocatalyst presents a copper concentration of 15.4 wt%. The introduction of Pt led to a decrease in the Cu loading (9.1–12.1 wt%) due to the controlled galvanostatic displacement of Cu^0 atoms by Pt^{4+} ions during the synthesis of CuPt/C catalyst. The total metal loading (Cu+Pt) rises from 11 to 19 wt% as the Cu atomic ratio decreases due to an increase in platinum. Moreover, ICP results reveal that the Cu:Pt atomic ratio is close to the nominal values for all the materials.

The size and distribution of metal nanoparticles was characterised by TEM. Fig. 1 shows the bright-field (TEM) and dark-field (HAADF-STEM) images of two selected CuPt/C catalysts (CuPt-99:1/C and CuPt-95:5/C) and the monometallic Cu/C. In general, a good distribution of metal nanoparticles onto the carbon support was observed for the samples. The mean particle size was below 2–3 nm, but the presence of a few larger particles is also noteworthy (dark-field images in Fig. 1). This large particle fraction is more important for the monometallic Cu/C catalyst, suggesting that Pt introduction leads to better particle size control. Particle size distributions (PSD) based on the examination of at least 100 particles from different STEM images highlight the most frequent particle sizes for each catalyst, with average sizes of 2.5, 1.8 and 1.3 nm for Cu/C, CuPt-99:1/C and CuPt-95:5/C, respectively (Fig. 1 and Figure S1). EDX analysis of CuPt/C catalysts confirmed the presence of both Cu and Pt for this fraction of small nanoparticles (Figure S2). These results indicate the coexistence of two phases in the CuPt/C catalysts: i) a high fraction of small and well-defined CuPt nanoparticles and ii) a lower contribution of larger copper (or CuO_X) nanoparticles.

Deeper insights into the morphology and structure were obtained by AC-HAADF-STEM for the catalyst with the highest Cu:Pt atomic ratio, which exhibited the highest selectivity for formate production at mild potentials (as will be seen later in Section 3.3.3). AC-HAADF-STEM image in Fig. 2 **(a)** shows a homogeneous distribution of CuPt nanoparticles with an average size ~ 2 nm. EDX analysis (Fig. 2 **(a)**, inset) indicates a Cu:Pt atomic ratio of 67:33, consistent with the values

Table 1
Cu:Pt atomic ratios, Cu and Pt concentrations and total metal loading determined from ICP and average crystal sizes of Cu phases identified by XRD for the CuPt/C electrocatalysts.

Catalyst	Cu:Pt ratio (at%:at%)	Cu (wt %)	Pt (wt %)	Cu+Pt (wt%)	Cu_2O (nm)	CuO (nm)
Cu/C	100:0	15.4	-	15.4	20.7	3.0
CuPt−99:1/C	98.5:1.5	10.2	0.5	10.7	-	3.4
CuPt−95:5/C	94.3:5.7	10.4	2.0	12.4	25.1	8.2
CuPt−90:10/C	90.1:9.9	12.1	4.1	16.2	7.9	6.8
CuPt−75:25/C	75.1:24.9	9.1	9.3	18.4	22.6	-

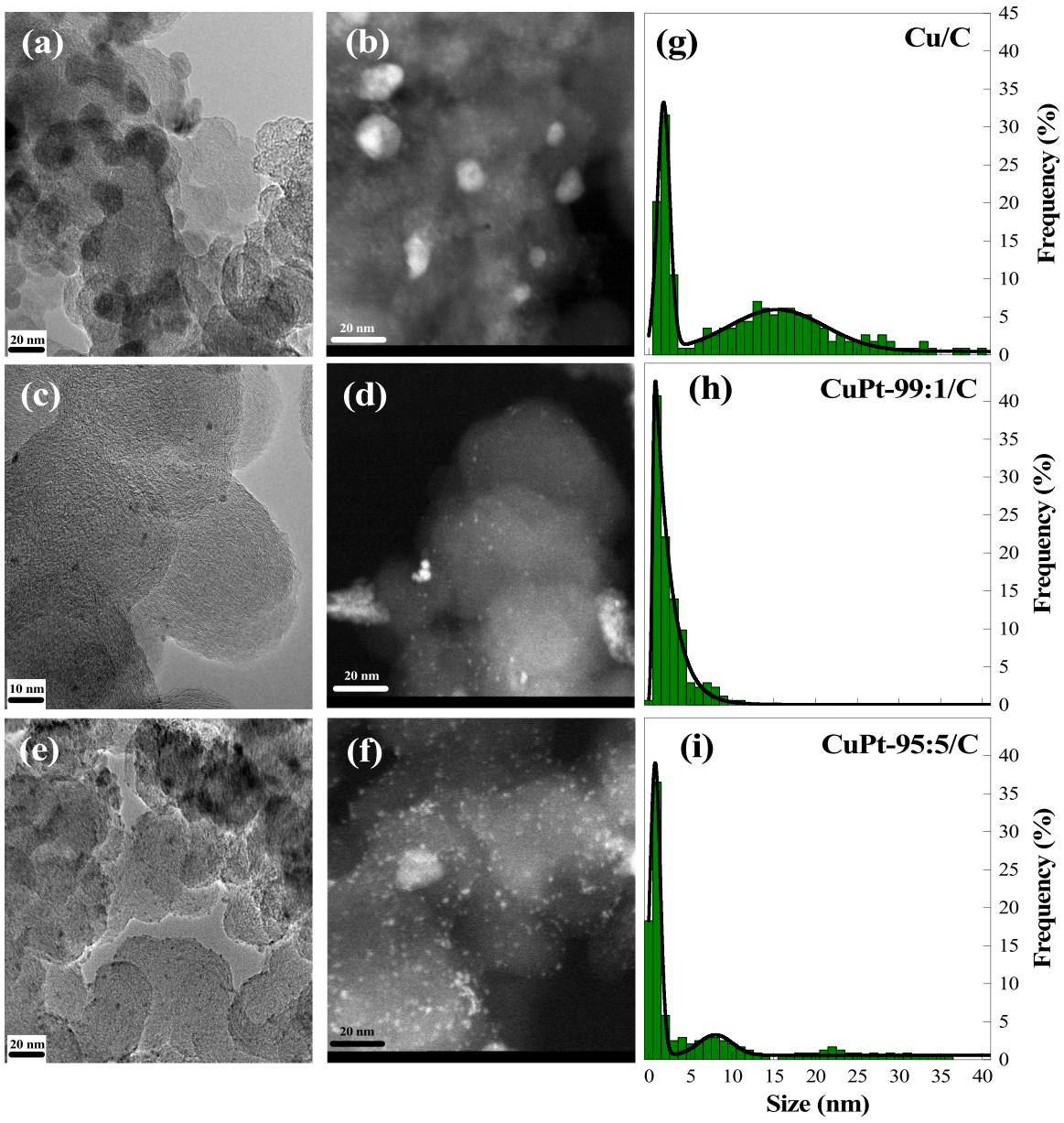


Fig. 1. TEM (left) and HAADF-STEM images (right) of: (a, b) Cu/C, (c,d), CuPt-99:1/C and (e,f) CuPt-95:5/C. (g, h, i) The corresponding particle size distributions.

obtained by XPS for CuPt-99:1/C (see later Fig. 3 **(b)**). As an example, Fig. 2 **(b)** illustrates different atomic contrasts in a CuPt nanoparticle due to the presence of Cu and Pt. Structural information of the nanoparticles was obtained from the corresponding fast Fourier transform (FFT) (inset in Fig. 2 **(b)**). The crystal structure was confirmed as fcc with interplanar distances of 0.214 nm and 0.188 nm, corresponding to (1 1 1) and (2 0 0) planes of CuPt alloys [49–51]. Likewise, EDX elemental mapping images showed a homogenous distribution of Cu and Pt atoms in the bimetallic nanoparticles (Figure S3).

The XRD patterns of synthesised catalysts are shown in Fig. 3 **(a)**. The monometallic Cu/C pattern exhibits five characteristic peaks at 2θ of 29.65°, 36.5°, 42.4°, 61.3°, 73.74° corresponding to the (1 1 0), (1 1 1), (2 0 0), (2 2 0), and (3 1 1) planes of cuprite Cu_2O, respectively. These peaks are also partially recognisable for CuPt-95:5/C, CuPt-90:10/C, and CuPt-75:25/C. The introduction of Pt led to the formation of Cu(II) phase, as evidenced by the peaks observed at 2θ = 35.5°, 38.7°, and 61.5° for the CuPt catalysts, assigned to the (0 0 2), (1 1 1), and (-1 1 3) Miller indices of tenorite CuO. Platinum reflections are discernible only in the CuPt-75:25/C sample, which exhibits a nearly amorphous structure with a much broader pattern, possibly due to the presence of tiny nanoparticles. In addition, CuO peaks are not evident in this last catalyst. In all diffractograms, a broad diffraction appears at 2θ of 26°, associated with (0 0 2) graphite, indicating a certain degree of graphitisation of the carbon support.

The average crystallite sizes of Cu_2O and CuO for the synthesised catalysts are presented in Table 1. The crystallite sizes of Cu_2O correlate well with large particle sizes (> 10 nm) observed by STEM for Cu/C and CuPt/C catalysts (Fig. 1, PSD). Moreover, a contribution centred at ~ 2.5, 3.5, and 7.5 nm is observed in the PSD of Cu/C, CuPt-99:1, and CuPt-95:5 (Fig. 1 and Figure S1), respectively, which is in line with CuO crystallite sizes (3.0, 3.4 and 8.2 nm). It is worth noting that CuPt nanoparticles identified by a combination of STEM and EDX (Fig. 3 and Figure S2) cannot be characterised by XRD since they are not large enough to present a crystal pattern.

The near-surface chemical composition of Cu/C and CuPt/C catalysts was investigated by XPS. The surface composition is given in Table S1. The surface copper concentration of the monometallic Cu/C catalyst is 4.4 wt%, whereas CuPt/C catalysts exhibit Cu contents ranging from 3.8

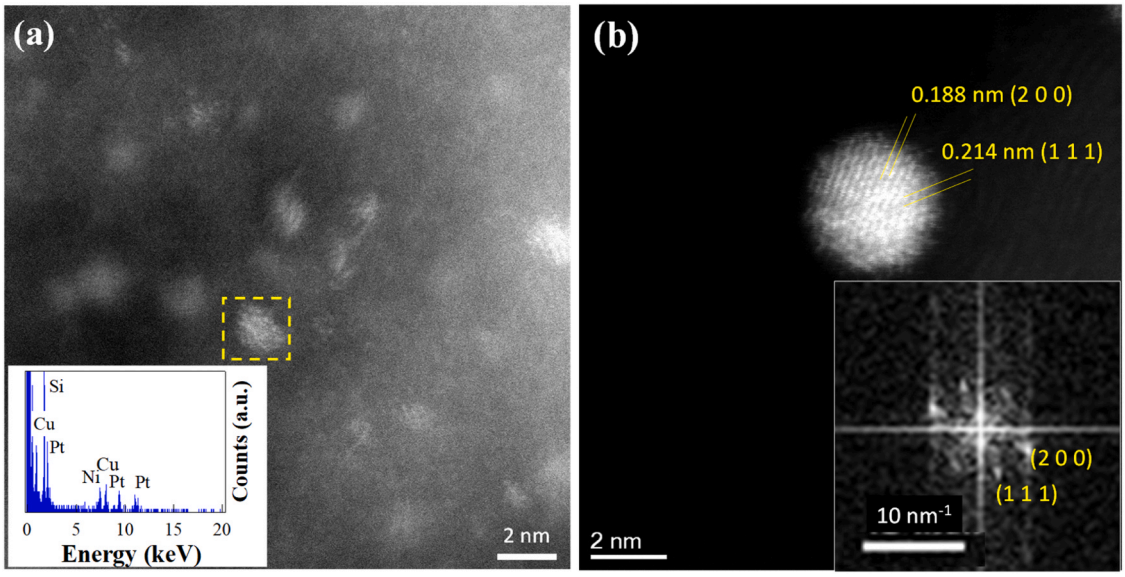


Fig. 2. (a) AC-HAADF-STEM image for CuPt-99:1/C catalyst. The inset shows the EDX analysis of the selected region (b) AC-HAADF-STEM image showing a single CuPt nanoparticle and the corresponding FFT (inset).

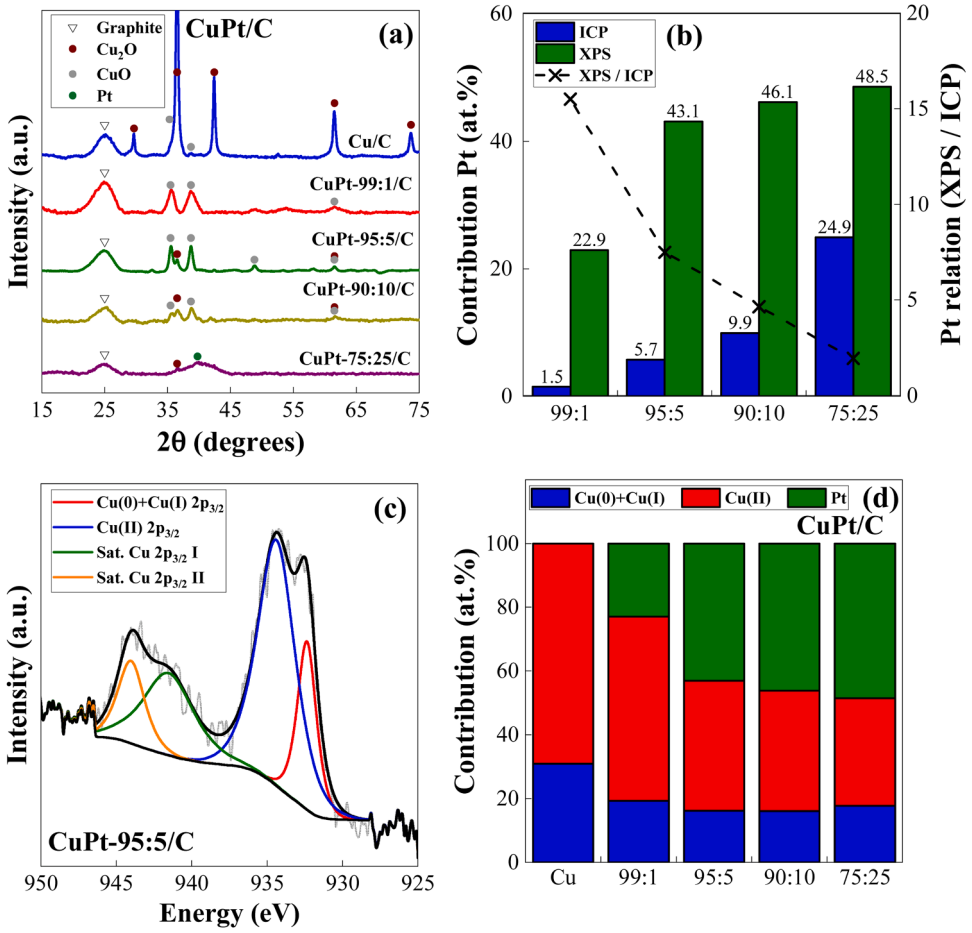


Fig. 3. (a) XRD patterns for the Cu/C and CuPt/C catalysts. References: graphite (JCPDS 41–1487), Cu_2O (JCPDS 77–0199), CuO (JCPDS 45–0937), and Pt (JCPDS 04–0802). (b) Platinum atomic contributions respect to the total metal amount (Pt/Cu+Pt), obtained by ICP-OES (blue bars) and XPS (green bars). Relation between the atomic contribution of platinum respect to the total metal amount determined by XPS and ICP (single points). (c) High-resolution XPS spectra of Cu $2p_{3/2}$ region for the CuPt-95:5/C catalyst. (d) Atomic contributions of Cu, Cu(0) + Cu(I) and Cu(II), from Cu $2p_{3/2}$ normalised to the copper content obtained by XPS $(Cu/(Cu+Pt))_{XPS}$. Pt contribution (at%) is also included $(Pt/(Cu+Pt))_{XPS}$.

to 8.6 wt%. The Pt concentration increases from 5.6 wt% for the CuPt-99:1/C catalyst to 25.0 for the catalyst with the lowest Cu:Pt atomic ratio. Fig. 3 **(b)** compares the Pt atomic contribution with respect to the total metal content obtained from ICP, $(Pt/(Cu+Pt))_{ICP}$, and XPS, $(Pt/(Cu+Pt))_{XPS}$, for the CuPt/C catalysts. While the ICP results are consistent with the nominal Pt atomic contributions, the XPS values are larger, indicating a significant enrichment of platinum on the surface of CuPt/C catalysts. Fig. 3 **(b)** also illustrates the ratio between surface and bulk platinum with respect to the metal content, $(Pt/(Cu+Pt))_{XPS}/(Pt/(Cu+Pt))_{ICP}$. This ratio decreases with the reduction of the Cu:Pt atomic ratio from 15.5 for the CuPt-99:1/C to 1.9 for the CuPt-75:25/C. This trend indicates the preferential enrichment of Pt in the surface of the catalysts for the highest Cu:Pt atomic ratios, CuPt-99:1/C and CuPt-95:5/C.

High-resolution XPS spectra of the Cu $2p_{3/2}$ region were deconvoluted into two contributions: i) the combination of Cu(0) and Cu(I) species centred at 932.5 ± 0.4 eV and ii) Cu(II) species centred at 933.6 ± 0.2 eV with two shake-up satellites at higher binding energies (941.1 ± 0.5 eV and 943.5 ± 0.5 eV, respectively) [52]. A rigorous resolution between Cu(0) and Cu(I) was not possible because of the overlap of peaks for these two components due to the relevant amount of Cu(II) [47]. As an example, the deconvoluted Cu $2p_{3/2}$ spectrum of the CuPt-95:5/C catalyst is shown in Fig. 3 **(c)**. The complete set of results is provided in the Supplementary Information (Figure S4).

Fig. 3 **(d)** illustrates the contribution of Cu(0)+Cu(I) and Cu(II) species of the synthesised catalysts, normalised to the atomic Cu contribution obtained by XPS, $(Cu/(Cu+Pt))_{XPS}$. Additionally, the contribution of platinum, $(Pt/(Cu+Pt))_{XPS}$, is also included in Fig. 3 **(d)**. A significant presence of Cu(II) is observed in all cases. Interestingly, the contribution of Cu(II) species decreases as the Cu:Pt atomic ratio decreases, while the presence of Cu(0)+Cu(I) is constant for the CuPt/C catalysts. In particular, the Cu(II) proportion gradually decreases from 57.9 % in CuPt-99:1/C catalysts to 33.8 % in CuPt-75:25/C. This trend is attributed to the synthesis method used to prepare CuPt nanoparticles through galvanic displacement of Cu(0) by Pt(IV)-ions. As a lower amount of platinum precursor is added during the synthesis of the catalysts, a lower fraction of Cu(0) atoms interact with Pt(IV)-ions. This leads to a higher amount of non-alloyed copper on the carbon support,

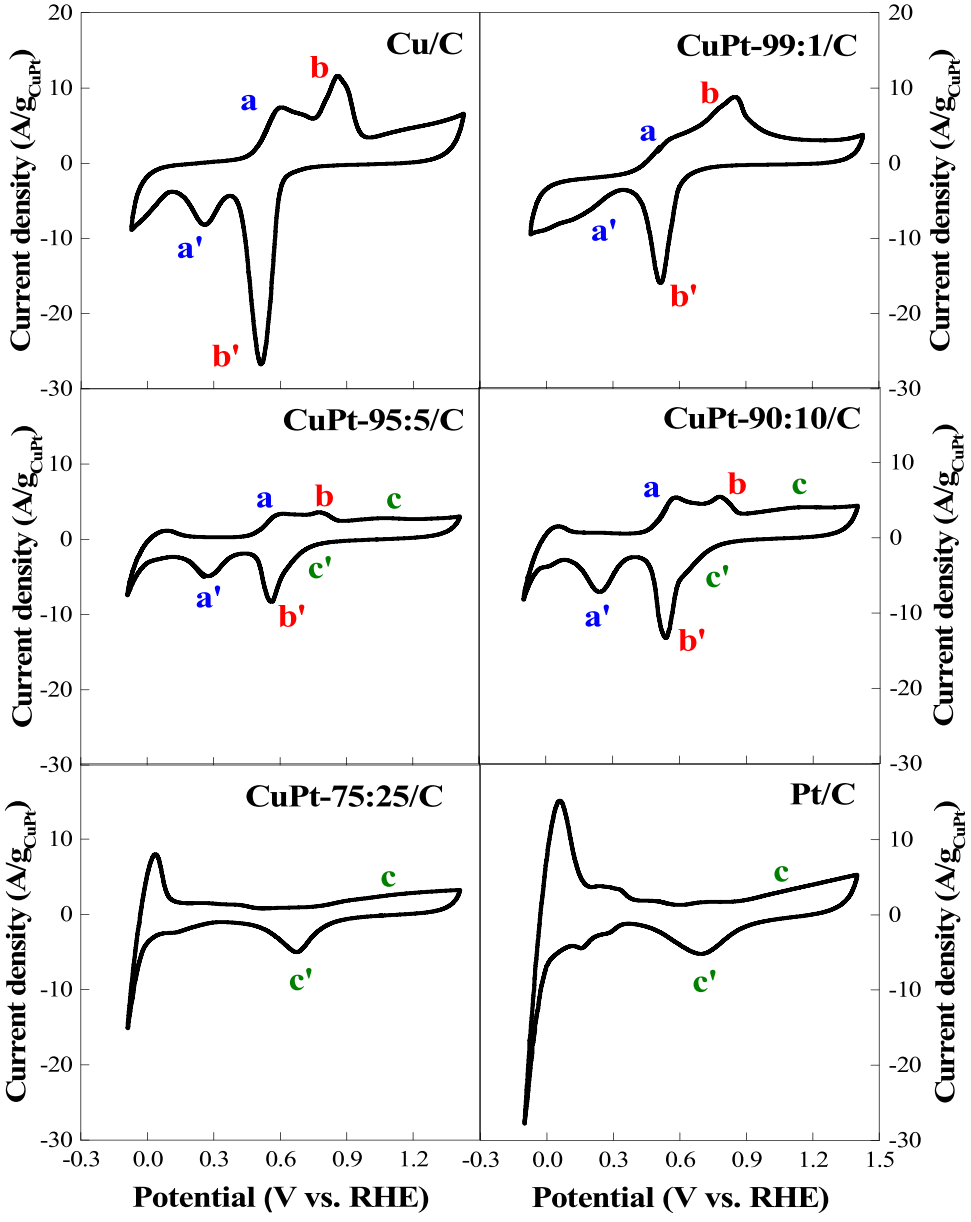


Fig. 4. CVs at 10 mV s^{-1} of CuPt/C, Cu/C, and commercial Pt/C catalysts in N_2-saturated 0.1 M $KHCO_3$.

which may subsequently oxidise under atmospheric conditions.

3.2. Electrochemical characterisation of the Cu/C and CuPt/C catalysts

First, the electrocatalytic activity towards the CO_2RR of CuPt/C and Cu/C catalysts was investigated using a glassy carbon electrode modified with a thin layer of the corresponding sample. The same experiments were also conducted using a commercial Pt/C catalyst (40 wt%, JM) as a monometallic Pt reference. Then, experiments in H-cell configuration were carried out to characterise the products derived from CO_2RR.

3.2.1. Cyclic voltammetry studies

The electrochemical behaviour of the catalysts was initially assessed by cyclic voltammetry in 0.1 M $KHCO_3$. Fig. 4 shows the cyclic voltammograms (CVs) recorded at a scan rate of 10 mV s^{-1} in the N_2-saturated electrolyte for the CuPt/C, Cu/C and Pt/C.

The CV of the monometallic Cu/C catalyst shows two distinct oxidation peaks: peak *a* (at 0.6 V vs. RHE) corresponds to the oxidation of Cu(0) to Cu(I), while peak *b* (at 0.85 V vs. RHE), represents the transition from Cu(I) to Cu(II). During the reverse potential scan, Cu(II) and Cu(I) are reduced to Cu(I) and Cu(0) at approximately 0.5 V vs. RHE (peak *b'*) and 0.26 V vs. RHE (peak *a'*), respectively [53,54]. On the other hand, the commercial Pt/C voltammogram shows that platinum is oxidised at around 1.0 V vs. RHE (peak *c*) and reduced back at 0.7 V vs. RHE (peak *c'*). CuPt/C catalysts show intermediate current-potential curves, demonstrating a gradual transition from copper- to platinum-like behaviour. Indeed, Cu-characteristic peaks (*a*, *a'*, *b*, and *b'*) are discernible in CuPt-99:1/C, CuPt-95:5/C, and CuPt-90:10/C catalysts, while are not evident for the Pt-richest catalyst (CuPt-75:25/C). In contrast, a sharp *c'* contribution (related to the reduction of Pt oxide) appears in the CV of CuPt-75:25/C catalyst, whereas it is not evident for CuPt-99:1/C. At potentials more negative than 0 V vs. RHE, the hydrogen evolution reaction initiates, being particularly pronounced in the Pt-richest catalyst (CuPt-75:25/C) and the monometallic Pt/C [55].

The activity for the CO_2RR of the CuPt/C catalysts was evaluated by LSV in the N_2- and CO_2-saturated electrolytes. Fig. 5 **(a)** shows the results for the CuPt-95:5/C catalyst. The reduction current density in the N_2-saturated 0.1 M $KHCO_3$ solution is only associated with the HER. After CO_2 bubbling, the faradaic current density is related to the simultaneous evolution of HER and CO_2RR. A reduction peak appears in the CO_2-saturated electrolyte centred at ~ −0.6 V vs. RHE. Moreover, the faradaic currents are more significant (negative) in the absence of dissolved CO_2. This behaviour is attributed to the reduction of CO_2 to $(CO_2)_{red}$ species, which adsorb onto the active phase of the catalyst, inhibiting the HER [56–58]. This current inhibition in the CO_2-saturated electrolyte is evident for all catalysts studied in this work (see later Fig. 5 **(c)**).

Fig. 5 **(b)** compares the LSV of all the catalysts under CO_2 saturation. The cathodic current density increases as the catalysts are richer in platinum, with CuPt-75:25/C displaying an electrochemical behaviour similar to the Pt/C catalyst. Platinum is well known to be a highly effective catalyst for the HER. Thus, higher hydrogen evolution is obtained as the catalyst is enriched in platinum (see LSV of the as-synthesised catalysts in the N_2-saturated electrolyte, Figure S5). Therefore, the increase of the current density as the Cu:Pt atomic ratio decreases is mainly related to an enhancement of the HER rate and not to the reduction of CO_2. Interestingly, CuPt/C catalysts with an atomic ratio Cu:Pt of 99:1 and 90:10 present an analogous behaviour to CuPt-95:5/C with a maximum of the current density at ~-0.6 V vs. RHE.

Fig. 5 **(c)** compares the ratio of the current densities (in absolute value) registered at −0.6 V under CO_2 and N_2 saturation for all the catalysts. A ratio below 1 was obtained for all the catalysts, reinforcing the statement that HER is inhibited during CO_2RR. Moreover, the current densities are further inhibited in catalysts with low or no platinum

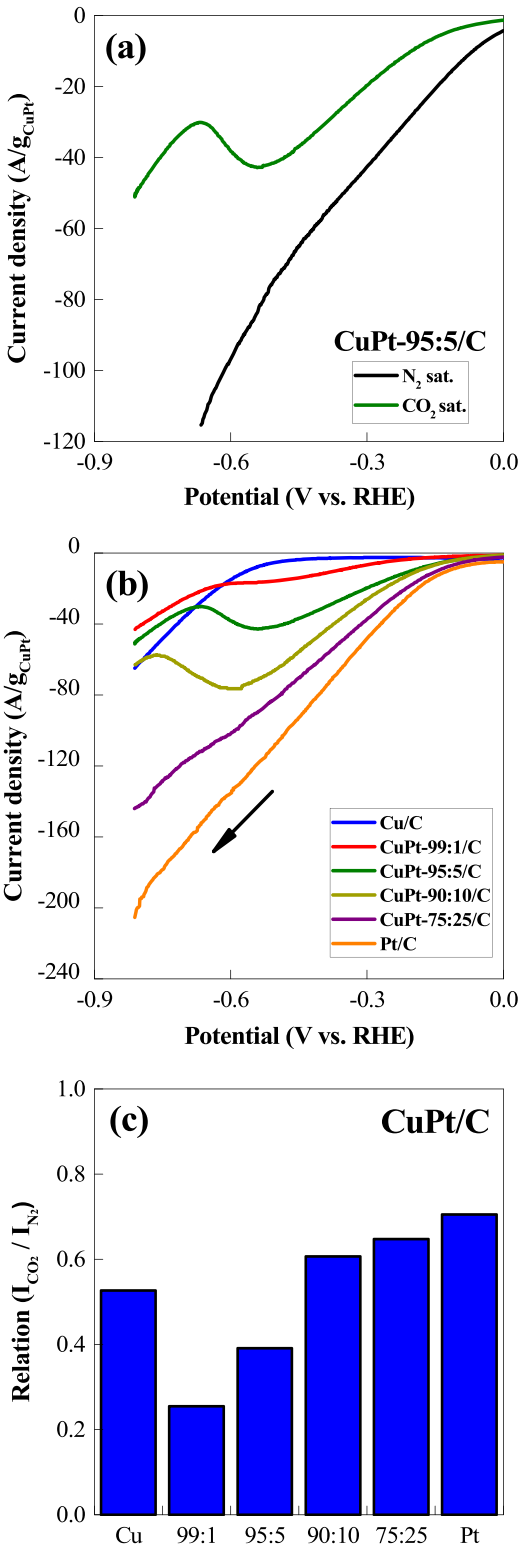


Fig. 5. (a) LSVs at 10 mV s^{-1} in N_2-saturated and CO_2-saturated 0.1 M $KHCO_3$ for CuPt-95:5/C. (b) Comparison of the LSVs at 10 mV s^{-1} in CO_2-saturated 0.1 M $KHCO_3$ for CuPt/C catalysts and the monometallic Cu/C and Pt/C. (c) Relationship between the currents recorded at −0.6 V during LSVs at 10 mV s^{-1} in N_2-saturated and CO_2-saturated in 0.1 M $KHCO_3$.

content, such as Cu/C, CuPt-99:1/C, and CuPt-95:5/C, progressively increasing with platinum content. This relationship implies hydrogen evolution is more strongly promoted with a higher platinum content.

3.2.2. *Further insights on the nature of adsorbed species during CO_2RR*

Further research into the nature of species adsorbed on CuPt/C catalysts, Cu/C, and Pt/C materials was conducted by CO_2 reduction/adsorption experiments and subsequent electrochemical oxidation of the adsorbed species.

For this purpose, the 0.1 M $KHCO_3$ electrolyte was saturated with CO_2 and then a potential of −0.6 V vs. RHE was applied for 15 minutes. After that, dissolved CO_2 was removed from the electrolyte by bubbling N_2 for 30 minutes. CVs were then recorded between −0.7 V and 1.4 V vs. RHE at a scan rate of 10 mV s^{-1}. The same experiments were also conducted under CO (98 %, Air Liquide) since it is an important intermediate during the CO_2RR. Fig. 6 **(a)** shows the CVs obtained for the catalyst CuPt-95:5/C after CO_2 (blue line) and CO (green line) reduction. The CV in the N_2-saturated 0.1 M $KHCO_3$ electrolyte in a potential window where CO_2RR does not occur is also included (black line, denoted as blank CV). At −0.6 V vs. RHE, CO_2 or CO molecules are reduced, forming intermediate species adsorbed on the catalyst surface. During the first anodic sweep, these adsorbates derived from CO_2 or CO reduction are oxidised in a potential window from 0.3 to 1.2 V vs. RHE, as can be seen in Fig. 6 **(a)** (inset). The results for all catalysts are displayed in Figure S6. Fig. 6 **(b)** shows the oxidation charges normalised per mass of metal [Q g_{CuPt}^{-1}] of the adsorbates derived from CO_2 (Q_{CO2}, green bars) and CO reduction (Q_{CO}, blue bars) for all the catalysts. These oxidation charges were determined by integrating the oxidation current densities after subtracting the area of the blank CV. The ratio between the oxidation charges associated with reduced/adsorbed CO_2 and reduced/adsorbed CO are also plotted as single points in Fig. 6 **(b)**.

The generally accepted mechanism for CO_2RR in aqueous solutions involves two main pathways: one leading to oxygen-bound intermediate (through one or two oxygen atoms, *OCHO), resulting in the production of formate, and the other involving *CO (via *COOH intermediate), which can either desorb as CO or continue evolving into other products [19,59]. Formate production can also occur via *COOH intermediate. A representative scheme of the generally accepted mechanism is shown in Fig. 7.

Considering both CO_2RR routes, the relationship between the charges assessed under CO and CO_2 saturation ($\chi = Q_{CO}/Q_{CO2}$ x 100) corresponds to the oxidation of the reduced and adsorbed intermediates through the CO pathway. Notably, these reduction/adsorption experiments exclude the desorbed species (not irreversibly adsorbed at the catalyst surface) derived from CO_2 or CO reduction at −0.6 V vs. RHE.

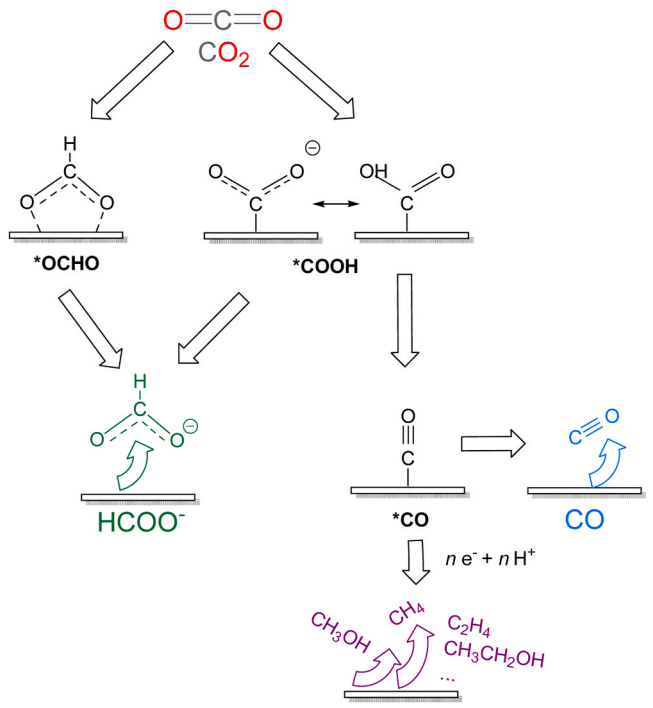


Fig. 7. Generally accepted mechanism for CO_2RR into CO and formate in aqueous solutions. Further reduction products are obtained from adsorbed CO (*CO).

Generally, oxidation charges relative to CO_2 or CO reduction/adsorption increase as the Cu:Pt atomic ratio decreases, which can be attributed to the platinum affinity for adsorbing carbon-bound intermediates (such as *COOH or *CO) [25]. As widely reported in the literature [24,60], Cu/C catalyst promotes the CO_2RR primarily via the CO route, resulting in similar oxidation charges for CO and CO_2 (χ = 94 %). The introduction of Pt leads to a decrease in the ratio between CO and CO_2 oxidation charges for CuPt-99:1/C and CuPt-95:5/C with χ values of 70–72 %, evidencing a promotion of adsorbates from the

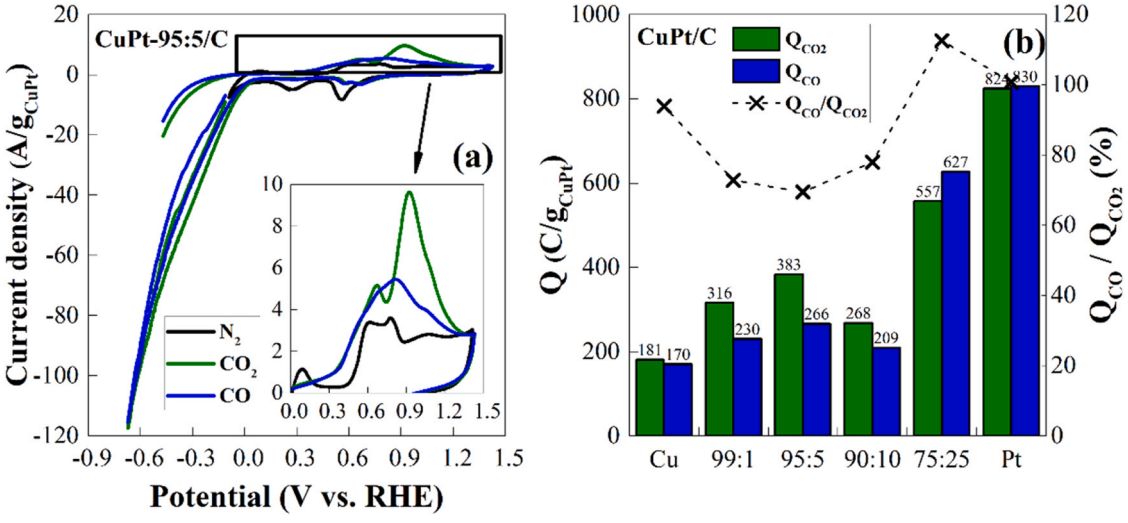


Fig. 6. CVs after reduction of CO_2 (green line) or CO (blue line) at −0.6 V vs. RHE for 15 minutes and posterior N_2 purge of the 0.1 M $KHCO_3$ electrolyte. (Inset) Zoomed-in view of the electrochemical oxidation of adsorbed species generated from CO_2 (green line) and CO (blue line) reduction at −0.6 V vs. RHE. (b) The corresponding oxidation charges (bars) for the CuPt/C catalysts and Cu/C and Pt/C. Relationship between the CO and CO_2 charges (single points).

formate pathway compared to Cu/C. This can be explained by a higher formation of adsorbed hydrogen (H_{ads}) on the surface of CuPt/C catalysts at mild potentials compared to Cu/C. The great H_{ads} coverage at the catalyst promotes the formate pathway presumably via an oxygen-bound intermediate (*OCHO) [25,61]. As the Cu:Pt atomic ratio decreases, the reduction and adsorption of species from the formate pathway is mitigated, especially for the Pt-enriched catalyst (CuPt-75:25/C). This is explained by the high coverage of Pt at this catalyst surface. This noble metal exhibits an excellent affinity for adsorbing *CO (from *COOH intermediate), which may poison the electrocatalytic surface and inhibit further reduction [62].

3.3. Product characterisation in an H-cell

The H-type electrochemical cell was coupled with an online gas chromatograph to characterise the electrocatalytic selectivity and product distribution of the synthesised catalysts. The electrocatalytic performance for CO_2RR was evaluated by chronoamperometry (CA) at some selected potentials, ranging from −0.6 V to −0.9 V vs. RHE.

The selectivity for CO_2RR products was assessed for all catalysts at the different potentials. Fig. 8 **(a, b, and c)** shows the results for Cu/C, CuPt-99:1/C, and CuPt-95:5/C, while Figure S7 presents the results for CuPt-90:10/C and CuPt-75:25/C. CO_2 reduction in Cu/C catalyst leads to a high selectivity for CO together with the production of formate, and in a lower contribution methane, C_2 compounds (ethylene, ethanol), and

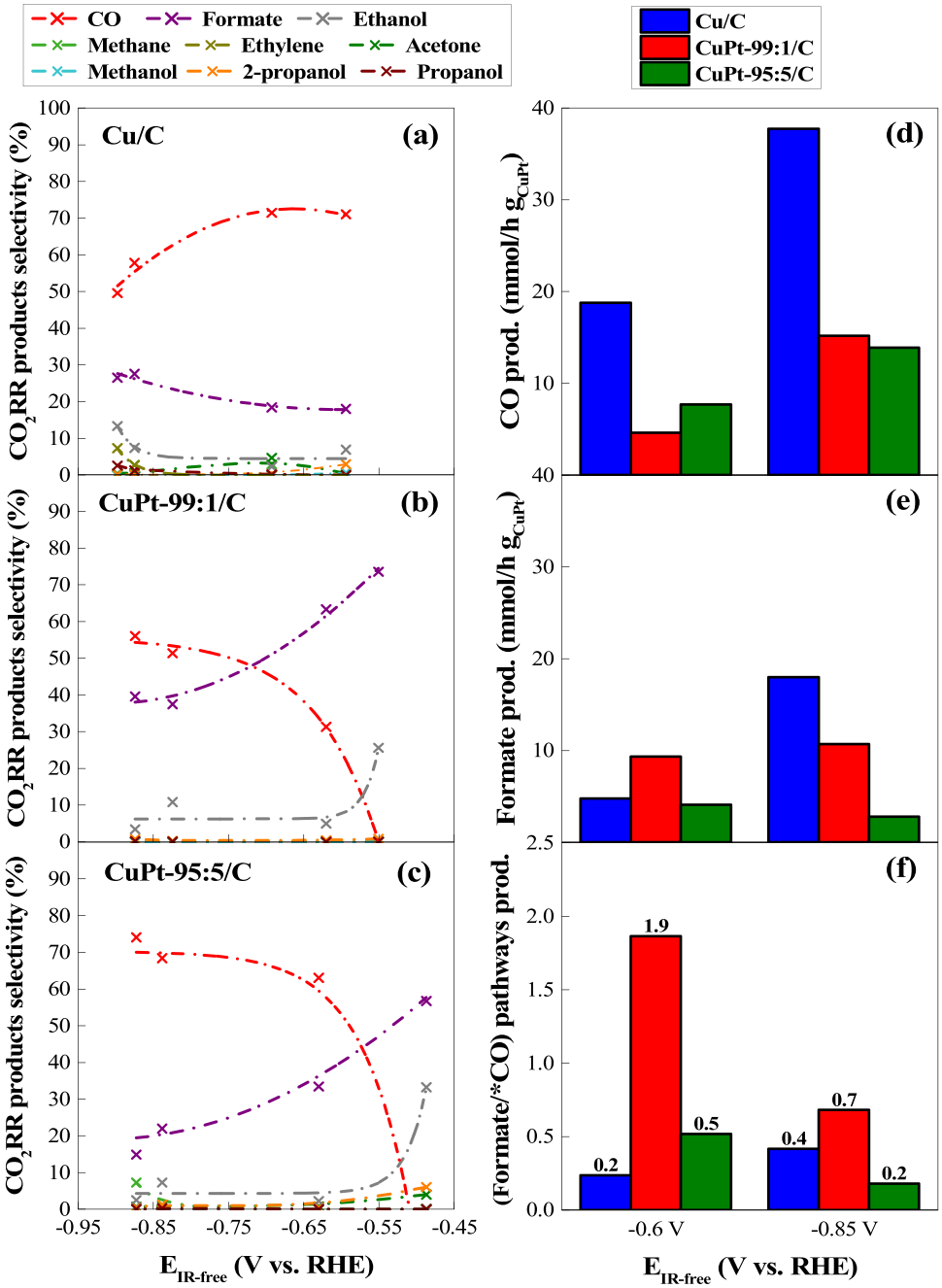


Fig. 8. Selectivity to CO_2RR products in the Cu/C, (a) CuPt-99:1/C, (b) and CuPt-95:5/C, (c) catalysts at the potentials analysed. (d) CO and (e) formate production by Cu/C, CuPt-99:1/C, and CuPt-95:5/C catalysts at −0.6 and −0.85 $V_{IR\text{-}free}$ vs. RHE potentials. (f) Relationship between formate and the products derived from CO pathway a for Cu/C, CuPt-99:1/C, and CuPt-95:5/C catalysts at the analysed potentials.

C_3 compounds (acetone, 1-propanol, and 2-propanol). When a low amount of platinum is introduced in the CuPt/C catalysts, the selectivity shifts primarily to formate, CO, and ethanol, with a negligible contribution from other products. At Cu:Pt atomic ratios lower than 95:5 (CuPt-90:10/C and CuPt-75:25/C catalysts), no notable changes in CO_2 selectivity are observed, indicating that higher platinum content does not substantially affect product selectivity (Figure S7).

Interestingly, the introduction of Pt alters product distribution, boosting formate selectivity at potentials less negative than −0.6 V vs. RHE, especially for the Cu:Pt atomic ratios of 99:1 and 95:5. In the monometallic Cu/C catalyst, the selectivity to CO gradually decreases as the overpotential increases, while formate selectivity increases correspondingly. This trend is not observed in CuPt/C catalysts. At mild potentials (less negative than −0.6 V vs. RHE), CO selectivity is low (negligible in some cases) and formate selectivity exceeds 50 %. CO selectivity rises sharply as the potential decreases, and formate selectivity drops significantly. These results evidence that the presence of platinum inhibits CO selectivity at mild potentials, enhancing formate selectivity.

Fig. 8 **(d and e)** illustrates the CO and formate production rates by the Cu/C, CuPt-99:1/C, and CuPt-95:5/C catalysts at two selected potentials (-0.6 and −0.85 V vs. RHE). At −0.6 V vs. RHE, CO production rate is significantly inhibited as platinum is introduced in the catalysts, while the formate production rate is similar for the Cu/C and CuPt/C catalysts, or even higher in the case of CuPt-99:1/C. Specifically, CO production is 18.8 mmol h^{-1} g_{Cu}^{-1} for the Cu/C catalyst, whereas it is drastically reduced to 4.6 mmol h^{-1} g_{CuPt}^{-1} and 7.7 mmol h^{-1} g_{CuPt}^{-1} for CuPt-99:1/C and CuPt-95:5/C, respectively (Fig. 8 **(d)**). In contrast, formate production at −0.6 V vs. RHE ranges from 4.7 mmol h^{-1} g_{Cu}^{-1} for Cu/C to 9.3 mmol h^{-1} g_{CuPt}^{-1} for CuPt-99:1/C and 4.1 mmol h^{-1} g_{CuPt}^{-1} for CuPt-95:5/C (Fig. 8 **(e)**). On the other hand, the monometallic Cu/C catalyst presents a higher formate production than CuPt/C catalysts at −0.85 V vs. RHE. It is worth mentioning that the production rate at all catalysts is limited by low current density and faradaic efficiencies below 50 % for CO_2 reduction, which is mainly associated with hydrogen production. That may be due to the employed H-cell configuration. The low solubility of CO_2 in aqueous electrolytes at room conditions hinders CO_2RR rates due to mass transport limitations of CO_2 [63,64]. At the cathode of a gas-phase co-electrolyser system, the CO_2RR faradaic efficiency is expected to be favoured over hydrogen formation due to the significantly higher concentration of CO_2 (available on the catalyst surface) [65–68]. In addition, the catalyst loading coupled with an increase of the electrode dimension can be optimised to enhance the catalyst's activity and the residence time toward higher CO_2RR rates. However, these aspects are beyond the scope of the present work.

Fig. 8 **(f)** shows the relationship between the production of formate and the products derived from the *CO pathway (including CO, CH_4, CH_3OH, CH_3CH_2OH, etc.) to illustrate the preferential formation of formate better. The preferential formation of formate is envisaged in the CuPt-99:1/C catalyst, with formate/*CO ratio of 1.9 at −0.6 V vs. RHE. While the CO route is favoured in Cu/C catalyst (especially at mild potential with a formate/*CO ratio of 0.2), the introduction of platinum suppresses the CO pathway and promotes the formate route. However, at more negative potentials, such as −0.85 V vs. RHE, the production of CO and CO-derived products increases in all catalysts, reducing the formate/*CO ratio with values in the range 0.2–0.7. These results show that the introduction of Pt promotes formate production at mild potentials, while CO is the main product at higher overpotentials. Moreover, formate production is boosted for the CuPt/C catalyst with the highest Cu:Pt atomic ratio studied in this work (CuPt-99:1/C).

To assess the stability issue commonly associated with copper catalysts, the current response of the optimum electrode during CO_2 electrolysis was evaluated through chronoamperometric testing over 22 hours in 0.1 M $KHCO_3$, at a potential where the formate pathway is promoted (-0.6 V vs RHE). The monometallic Cu/C catalyst was also included for comparison. No obvious degradation was observed for both electrodes over 22 hours under continuous CO_2RR, as evidences Figure S8. Cu/C electrode maintained a current density of ~ −5 A g_{Cu+Pt}^{-1}, while a higher value was obtained for the bimetallic CuPt-99:1/C (-8.5 A g_{Cu+Pt}^{-1}).

4. Discussion

The observation of $HCOO^-$ production at mild potentials is consistent with previous studies on CO_2-to-formate catalysts, such as those based on Sn and Bi [69–71]. Theoretical studies based on density functional theory (DFT) have shown that CO_2 conversion to formate can be promoted by the presence of adsorbed hydrogen. For instance, Sirijaraensre et al. affirmed that the presence of adsorbed hydrogen improves significantly the selectivity towards formate on a catalyst based on copper atoms embedded in graphene [72]. The preferential CO_2-to--formate pathway at moderate potentials has been also showed at Cu nanoparticles dispersed in a N-doped carbon, which was attributed to an enhancement in water activation due to the synergistic effect of N functionalities and highly dispersed ultrasmall Cu nanocrystals [67]. Similarly, Esrafili et al. demonstrated that Pt-doped-graphene is a promising catalyst for formate production due to the ability of Pt to activate H_2 [73]. Previous works have also reported enhanced formate production on bimetallic catalysts, such as CuPd/C [74] and PtPd surfaces [75,76]. The selective formate production was found to result from a low *CO coverage at the catalyst surface in benefit of a high hydrogen adsorption, which can react with formate intermediate (*OCHO). Based on this, the increase of the formate selectivity at mild potentials of CuPt/C catalysts in our work may be explained by the affinity of Pt to adsorb hydrogen. This effect is most pronounced in the CuPt-99:1/C catalyst at mild potentials (-0.6 V vs. RHE) with a CO_2RR selectivity to formate up to 74 % at −0.55 V vs. RHE (Fig. 8 **(b)**). At larger overpotentials (applied potential more negative than −0.7 V vs. RHE), this trend changes and CO is the main CO_2RR product, with a selectivity close to 56 % at −0.85 V for CuPt-99:1/C. In line with these results, Ye et al. showed a reduction in formate production at larger overpotentials on PdPt catalysts, due to high *CO coverage on the catalytic surface, which limits the stabilisation of CO_2 via the formate intermediate [76]. Fig. 9 illustrates that the preferential CO production occurs at lower overpotentials as the Cu:Pt ratio decreases, while formate production gradually decreases. In this context, CO_2RR selectivity to CO is close to 70 % at −0.6 V vs. RHE for the catalysts with the highest Pt contents (CuPt-75:25/C and CuPt-90:10/C) with formate accounting for the remaining 30 %. In contrast, CuPt-99:1/C and CuPt-95:5/C exhibit a formate selectivity of 65 % and 40 %, respectively, at the same potential.

Therefore, the formation of formate on CuPt/C catalysts is favoured at Cu:Pt atomic ratio above 95:5 and in particular at mild overpotentials (applied potentials less negative than −0.6 V vs. RHE). CO_2RR preferentially occurs via the CO* pathway at the monometallic Cu/C catalyst (see Fig. 8 **(a)**). The introduction of platinum reduces the reaction overpotential for CO_2 activation [39] and enhances water activation and thus, the availability of adsorbed hydrogen compared to monometallic Cu/C (see Fig. 5**b** and Figure S5). The latter facilitates the reduction of CO_2RR adsorbates to formate at the surface of CuPt alloy nanoparticles. *OCHO is well-known to be a key intermediate for formate production at transition metals, such as Cu or Pt [24,25]. However, formate production via *COOH intermediate [20,77,78] (see Fig. 7) or physisorbed CO_2 [79] cannot be discarded. Moreover, ethanol formation was also observed on CuPt/C at mild potentials. Based on these results, CuPt/C catalysts bind *OCHO strongly enough for formate production to dominate CO_2RR selectivity at mild potentials, but weakly enough to allow the further reduction of products through *CO (via *COOH intermediate). Other authors have reported similar results for Cu surfaces [25]. The reduction in CO_2RR to formate selectivity as the Cu:Pt ratio decreases or as the overpotential increases is likely due to the intermediate binding affinity of Pt for carbon-bound *COOH intermediate,

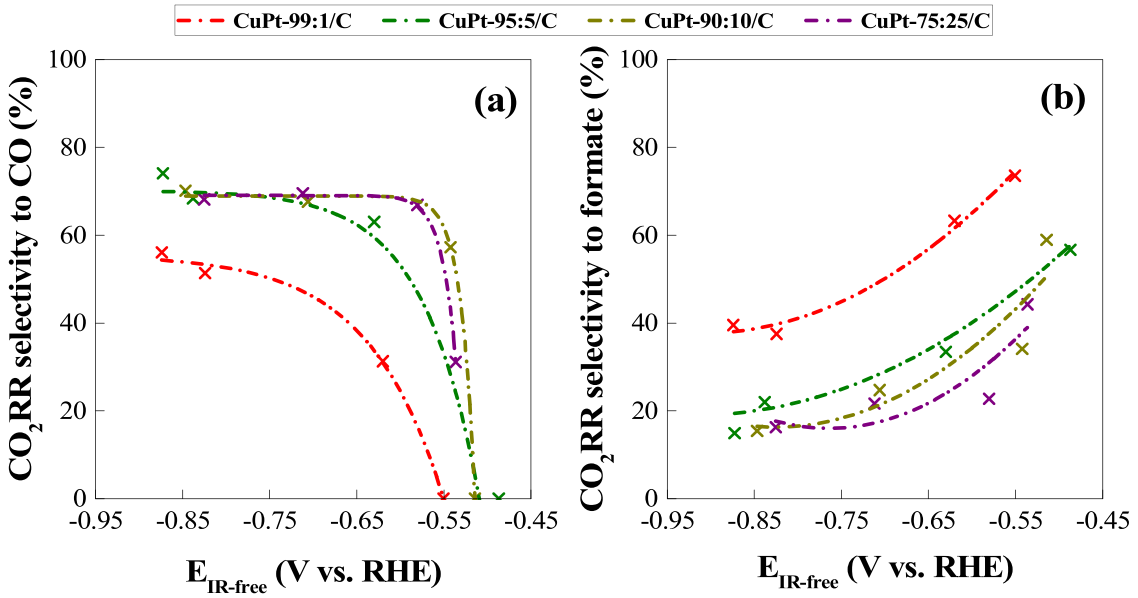


Fig. 9. CO_2RR selectivity for (a) CO (b) and formate products in CuPt-99:1/C, CuPt-95:5/C, CuPt-90:10/C, and CuPt-75:25/C catalysts at the analysed potentials.

which leads to the preferential formation of CO [80]. Therefore, CuPt-99:1/C (followed by CuPt-95:5/C), with a preferential enrichment of Pt at the surface of the catalyst (see Fig. 3 **(d)**), but with the lowest Pt loading, presented the best performance for formate production at mild potentials.

Moreover, differences in Cu oxidation state may also influence the selectivity for CO_2RR. Copper oxides have been proposed to play a critical role in electrochemical CO_2 conversion due to their high surface area, rough morphology, and significant defect density [80–86]. The XRD pattern (Fig. 3 **(a)**) of the best-performing catalyst for formate production, CuPt-99:1/C, discards the presence of Cu_2O crystals. This contrasts with findings from previous works on the efficient CO_2 reduction to formate over Cu_2O surfaces [87–89]. However, CuPt-99:1/C and CuPt-95:5/C catalysts exhibit the highest surface concentration of Cu(II) (determined by XPS, see Fig. 3 **(d)**) among the set of CuPt/C catalysts, coinciding with the highest formate production. That is consistent with previous studies demonstrating selective formate generation on CuO-based catalysts [77,90,91]. However, the enhancement of overall CO_2RR selectivity to formate cannot be entirely attributed to the presence of the CuO phase, as the monometallic Cu/C catalyst exhibited the largest surface atomic contribution of Cu(II) (69.1 % by XPS). Nevertheless, the selectivity for formate production at −0.65 V vs. RHE was lower than those obtained for CuPt-99:1/C and CuPt-95:5/C (see Fig. 8 **(f)**). On the other hand, when negative potentials are applied in the presence of CO_2, the oxides often undergo reduction to its metallic phase, forming nanostructured Cu through an in-situ transformation [84,92,93]. It is plausible that the reduced Cu phase can enhance the affinity for the oxygen-bound intermediate of CuPt nanoparticles in the presence of an appropriate Pt amount, in line with recent findings on Cu-Ag surfaces [93]. This behaviour would also contribute to the higher formate selectivity over the CuPt/C catalyst than over the Cu/C one. Thus, the contribution of Cu(II) and Cu(I) phases on the overall activity and selectivity for CO_2RR is expected to be limited. Moreover, TEM images (see Fig. 1) evidenced a main contribution of small CuPt nanoparticles, which coexist with larger copper oxide particles. As a potential avenue for future development, operando characterisation by X-ray absorption spectroscopy could unravel distinctive effects between CuPt alloys and CuO_X for CO_2RR at as-synthesised CuPt/C catalysts.

The results shown in Fig. 8 and Fig. 9 are consistent with the electrochemical behaviour observed in Fig. 5 **(b)**, where a cathodic peak appears at −0.5/-0.6 V vs. RHE for the catalysts with Cu:Pt atomic ratios from 99:1–90:10. This peak is likely related to CO_2RR via formate pathway. This contribution progressively diminishes in catalysts with the lowest Cu:Pt atomic ratio, suggesting significant CO poisoning. Similarly, the high *CO coverage dominates CO_2RR at higher overpotentials, preventing formate production and intensifying hydrogen formation by water reduction on available active sites. The results also align with the CO_2 reduction/adsorption experiments (Fig. 6), where the adsorption of species from the CO_2 reduction via the formate pathway is facilitated on catalysts with a lower platinum content. At Cu:Pt atomic ratios below 90:10, the high *COOH (and *CO) coverage blocks the active sites, inhibiting formate production.

These results demonstrate that the surface enrichment of platinum on Cu/C catalysts via galvanic displacement is an effective approach to reduce the required overpotential for CO_2 activation of copper and to promote formate production at mild potentials. To the best of our knowledge, this work is the first to report formate production on small CuPt nanoparticles supported on carbon at mild potentials. Previous works showed the preferential formation of CO and hydrocarbons using CuPt nanocubes [44,45]. Strasser et al. also found the formation of methane and ethylene over Cu overlayers of different nanometer-thickness deposited on Pt [94]. Similarly, the main production of CH_4 or C_2H_4 has been recently reported on PtCu single-atom alloys catalysts [43,95]. In our work, the change in the CO_2RR pathway at CuPt/C catalysts seem to be related to the size and shape of CuPt nanocrystals and the Cu:Pt atomic ratio. Thus, much further improvement in the CO_2-to-formate activity and selectivity could be achieved by controlling the particle size (for example varying the buffer pH during the synthesis of the particles) or tuning the Cu:Pt atomic ratio to values above 99:1. Moreover, the interaction of the carbon support and bimetallic nanoparticles may also influence the CO_2RR performance. Recent works found selective formate production at monometallic Cu or Pt nanoparticles supported on a N-doped carbon material due to an enhancement of water activation by the synergistic effect of N functionalities and the active nanocrystals [42,67]. The design of new CuPt using different carbon supports doped with nitrogen (or other heteroatoms) can be also explored for selective formate production. Although formate production on as-synthesised CuPt/C catalysts is modest compared to those obtained on p-block metal-based catalysts (Sn, Bi) [59], and these results are therefore illustrative, the present work clearly demonstrates the promotion of formate production on

CuPt-based catalysts at mild potentials. Further improvements in terms of current density and CO_2RR rates are expected in a continuous-flow CO_2 electrolyser operating with gas diffusion electrodes.

5. Conclusions

Herein, we investigated the influence of the Cu:Pt atomic ratio on the activity and selectivity for the CO_2 reduction reaction of CuPt/C catalysts. Physicochemical characterisation revealed a homogeneous distribution of CuPt nanoparticles of 1–2 nm, coexisting with CuO_x particles. The results revealed that introducing a well-controlled amount of platinum on Cu/C significantly impacted the CO_2RR performance. Cu:Pt catalysts with 99:1 and 95:5 at. ratios enhanced formate production over the products derived from the *CO reduction pathway, particularly at mild potentials (-0.6 V vs. RHE).

Platinum reduces the reaction overpotential for CO_2 activation compared to monometallic Cu/C and facilitates the presence of *H at bimetallic CuPt/C catalysts, favouring formate evolution. However, the increased *COOH coverage at more negative potentials or higher platinum contents, results in a decrease of formate production. Incorporating Pt via galvanic displacement of Cu/C catalysts can be explored to tune the CO_2RR selectivity of copper nanoparticles to formate production.

CRediT authorship contribution statement

Lázaro M. J.: Resources, Project administration, Investigation, Funding acquisition. **Pérez-Rodríguez Sara:** Writing – review & editing, Supervision, Project administration, Investigation, Funding acquisition, Conceptualization, Writing – original draft. **Gutiérrez-Roa M.:** Writing – original draft, Visualization, Methodology, Investigation, Formal analysis, Data curation. **Sebastián D.:** Writing – review & editing, Supervision, Project administration, Investigation, Funding acquisition, Conceptualization. **Gallone M.:** Investigation, Formal analysis. **Hernández S.:** Writing – review & editing, Resources, Investigation, Funding acquisition. **Guzmán H.:** Writing – review & editing, Investigation, Formal analysis. **Zammillo F.:** Investigation, Formal analysis.

Declaration of Competing Interest

The authors declare that they have no known competing financial interests or personal relationships that could have appeared to influence the work reported in this paper.

Acknowledgments

Authors acknowledge Grant PID2020–115848RB-C21 “STORELEC” project funded by MICIU/AEI/10.13039/501100011033 and Grant CNS2023–144433 “ALCOELECTRO” project funded by MICIU/AEI/10.13039/501100011033 and by the “European Union NextGenerationEU/PRTR”. Authors also acknowledge Gobierno de Aragón (DGA) for financially supporting *Grupo de Conversión de Combustibles* (T06_23R) and the project LMP253_21. Sara Pérez-Rodríguez thanks Grant IJC2019–041874-I funded by the MICIU/AEI/10.13039/501100011033. Manuel Gutiérrez-Roa acknowledges Universidad de Zaragoza, *Fundación Ibercaja* and Fundación CAI for the financial support IT 11/23 and *Programa Iberus+ : Movilidad para doctorandos* for his mobility grant. Simelys Hernández acknowledges the project CO_2Synthesis (ID ROL: 67910) funded by Fondazione Compagnia di San Paolo in the Call Trapezio - Linea 1. Federica Zammillo and Mario Gallone thanks Fondazione CRT for the financial support. Authors thank LMA at Universidad de Zaragoza for offering access to TEM/STEM facilities.

Appendix A. Supporting information

Supplementary data associated with this article can be found in the online version at doi:10.1016/j.jcou.2025.103084.

Data Availability

Data will be made available on request.

References

[1] P. Friedlingstein, M. O’Sullivan, M.W. Jones, R.M. Andrew, D.C.E. Bakker, J. Hauck, et al., Global Carbon Budget 2023, Earth Syst. Sci. Data 15 (12) (2023) 5301–5369, https://doi.org/10.5194/essd-15-5301-2.
[2] M. Yusuf, H. Ibrahim, A comprehensive review on recent trends in carbon capture, utilization, and storage techniques, J. Environ. Chem. Eng. 11 (5) (2023) 111–393, https://doi.org/10.1016/j.jece.2023.11139.
[3] E. García-Bordejé, R. González-Olmos, Advances in process intensification of direct air CO_2 capture with chemical conversion, Prog. Energy Combust. Sci. 100 (2024) 101–132, https://doi.org/10.1016/j.pecs.2023.101132.
[4] G. Yergaziyeva, Z. Kuspanov, M. Mambetova, N. Khudaibergenov, N. Makayeva, C. Daulbayev, Advancements in catalytic, photocatalytic, and electrocatalytic CO_2 conversion processes: current trends and future outlook”, *J. CO_2 Util.* 80 (2024) 102–682, https://doi.org/10.1016/j.jcou.2024.102682.
[5] O.S. Bushuyev, P. De Luna, C.T. Dinh, L. Tao, G. Saur, J. van de Lagemaat, et al., What should we make with CO_2 and how can we make it? Joule 2 (5) (2018) 825–832, https://doi.org/10.1016/j.joule.2017.09.003.
[6] S.C. Perry, P.-K. Leung, L. Wang, C. Ponce de León, et al., Developments on carbon dioxide reduction: their promise, achievements, and challenges, Curr. Opin. Electrochem. 20 (2020) 88–98, https://doi.org/10.1016/j.coelec.2020.04.014.
[7] A. Irabien, M. Alvarez-Guerra, J. Albo, A. Dominguez-Ramos, Electrochemical conversion of CO_2 to value-added products. Electrochemical water and wastewater treatment, Elsevier, 2018, pp. 29–59, https://doi.org/10.1016/B978-0-12-813160-2.00002-X.
[8] H. Jiang, L. Wang, Y. Li, B. Gao, Y. Guo, C. Yan, et al., High-selectivity electrochemical CO_2 reduction to formate at low overpotential over Bi catalyst with hexagonal sheet structure, Appl. Surf. Sci. 541 (2021) 148577, https://doi.org/10.1016/j.apsusc.2020.148577.
[9] M.F. Liu, C. Zhang, J. Wang, X. Han, W. Hu, Y. Deng, Recent research progresses of Sn/Bi/In-based electrocatalysts for electroreduction CO_2 to formate, Chem. A Eur. J. 30 (17) (2024) 1–19, https://doi.org/10.1002/chem.202303711.
[10] R. Shi, J. Guo, X. Zhang, G.I.N. Waterhouse, Z. Han, Y. Zhao, et al., Efficient wettability-controlled electroreduction of CO_2 to CO at Au/C interfaces”, Nat. Commun. 11 (1) (2020) 16847, https://doi.org/10.1038/s41467-020-16847-9.
[11] W.H. Lee, C. Lim, S.Y. Lee, K.H. Chae, C.H. Choi, U. Lee, et al., Highly selective and stackable electrode design for gaseous CO_2 electroreduction to ethylene in a zero-gap configuration, Nano Energy 84 (105859) (2021), https://doi.org/10.1016/j.nanoen.2021.105859.
[12] D. Gao, H. Zhou, J. Wang, S. Miao, F. Yang, G. Wang, et al., Size-dependent electrocatalytic reduction of CO_2 over Pd nanoparticles, J. Am. Chem. Soc. 137 (13) (2015) 4288–4291, https://doi.org/10.1021/jacs.5b00046.
[13] S. Pérez-Rodríguez, M. Gutiérrez-Roa, C. Giménez-Rubio, D. Ríos-Ruiz, P. Arévalo-Cid, M.V. Martínez-Huerta, et al., Single atom Cu-N-C catalysts for the electroreduction of CO_2 to CO assessed by rotating ring-disc electrode, J. Energy Chem. 88 (2024) 169–182, https://doi.org/10.1016/j.jechem.2023.09.00.
[14] K.P. Kuhl, E.R. Cave, D.N. Abram, T.F. Jaramillo, New insights into the electrochemical reduction of carbon dioxide on metallic copper surfaces, Energy Environ. Sci. 5 (5) (2012) 7050–7059, https://doi.org/10.1039/c2ee21234j.
[15] J. Yuan, M.P. Yang, W.Y. Zhi, H. Wang, H. Wang, J.X. Lu, Efficient electrochemical reduction of CO_2 to ethanol on Cu nanoparticles decorated on N-doped graphene oxide catalysts, J. CO_2 Util. 33 (2019) 452–460, https://doi.org/10.1016/j.jcou.2019.07.014.
[16] H. Tang, Y. Zhou, Y. Liu, Y. Qian, Z. Qiu, A. Chen, B.-L. Lin, Rationally designed hierarchical carbon supported CuO nano-sheets for highly efficient electroreduction of CO_2 to multi-carbon products, J. CO_2 Util. 67 (2023) 102320, https://doi.org/10.1016/j.jcou.2022.102320.
[17] H. Guzmán, N. Russo, S. Hernández, CO_2 valorisation towards alcohols by Cu-based electrocatalysts: challenges and perspectives, Green. Chem. 23 (2021) 1896–1920, https://doi.org/10.1039/d0gc03334k.
[18] M.P. Mezzapesa, F. Salomone, H. Guzmán, M. Castellino, A. Chiodoni, K. Bejtka, et al., Development of In-Cu binary oxide catalysts for hydrogenating CO_2 via thermocatalytic and electrocatalytic routes, Inorg. Chem. Front. 11 (8) (2024) 2319–2338, https://doi.org/10.1039/d3qi02499g.
[19] S. Nitopi, E. Bertheussen, S.B. Scott, X. Liu, A.K. Engstfeld, S. Horch, et al., Progress and perspectives of electrochemical CO_2 reduction on copper in aqueous electrolyte, Chem. Rev. 119 (12) (2019) 7610–7672, https://doi.org/10.1021/acs.chemrev.8b00705.
[20] A.A. Peterson, F. Abild-Pedersen, F. Studt, J. Rossmeisl, J.K. Nørskov, How copper catalyzes the electroreduction of carbon dioxide into hydrocarbon fuels, Energy Environ. Sci. 3 (9) (2010) 1311–1315, https://doi.org/10.1039/c0ee00071j.
[21] T. Ahmad, S. Liu, M. Sajid, K. Li, M. Ali, L. Liu, et al., Electrochemical CO_2 reduction to C_{2+} products using Cu-based electrocatalysts: a review, Nano Res. Energy 1 (e9120021) (2022) 1–14, https://doi.org/10.26599/NRE.2022.9120021.
[22] G. Wu, Y. Song, Q. Zheng, C. Long, T. Fan, Z. Yang, X. Huang, Q. Li, Y. Sun, L. Zuo, S. Lei, Z. Tang, Selective electroreduction of CO_2 to n-Propanol in two-step tandem catalytic system, Adv. Energy Mater. 12 (36) (2022) 2202054, https://doi.org/10.1002/aenm.202202054.

[23] H. Guzmán, D. Roldán, N. Russo, S. Hernández, Ultrasound-assisted synthesis of copper-based catalysts for the electrocatalytic CO_2 reduction: effect of ultrasound irradiation, precursor concentration and calcination temperature, Sustain. Mater. Technol. 35 (2023) e00557, https://doi.org/10.1016/j.susmat.2022.e00557.

[24] R. Kortlever, J. Shen, K.J.P. Schouten, F. Calle-Vallejo, M.T.M. Koper, Catalysts and reaction pathways for the electrochemical reduction of carbon dioxide, J. Phys. Chem. Lett. 6 (20) (2015) 4073–4082, https://doi.org/10.1021/acs.jpclett.5b01559.

[25] J.T. Feaster, C. Shi, E.R. Cave, T. Hatsukade, D.N. Abram, K.P. Kuhl, et al., Understanding selectivity for the electrochemical reduction of carbon dioxide to formic acid and carbon monoxide on metal electrodes, ACS Catal. 7 (7) (2017) 4822–4827, https://doi.org/10.1021/acscatal.7b00687.

[26] K. Fernández-Caso, G. Díaz-Sainz, M. Alvarez-Guerra, A. Irabien, Electroreduction of CO_2: advances in the continuous production of formic acid and formate, ACS Energy Lett. 8 (2023) 1992–2024, https://doi.org/10.1021/acsenergylett.3c00489.

[27] B. Ávila-Bolívar, R. Cepitis, M. Alam, J.-M. Assafrei, K. Ping, J. Aruväli, et al., CO_2 reduction to formate on an affordable bismuth metal-organic framework based catalyst, J. CO_2 Util. 59 (2022) 101937, https://doi.org/10.1016/j.jcou.2022.101937.

[28] H. Shen, Y. Zhao, L. Zhang, Y. He, S. Yang, T. Wang, et al., In-Situ constructuring of copper-doped bismuth catalyst for highly efficient CO_2 electrolysis to formate in ampere-level, Adv. Energy Mater. 13 (2023) 2202818, https://doi.org/10.1002/aenm.202202818.

[29] B.C. Marepally, C. Ampelli, C. Genovese, F. Tavella, L. Veyre, E.A. Quadrelli, et al., Role of small Cu nanoparticles in the behaviour of nanocarbon-based electrodes for the electrocatalytic reduction of CO_2, J. CO_2 Util. 21 (2017) 534–542, https://doi.org/10.1016/j.jcou.2017.08.00.

[30] Y. Fu, K. Leng, H. Zhuo, W. Liu, L. Liu, G. Zhou, et al., Nanoconfinement effects on $CuBi_3$ alloy catalyst for efficient CO_2 electroreduction to formic acid, J. CO_2 Util. 70 (2023) 102456, https://doi.org/10.1016/j.jcou.2023.102456.

[31] T. Zheng, C. Liu, C. Guo, M. Zhang, X. Li, Q. Jiang, et al., Copper-catalysed exclusive CO_2 to pure formic acid conversion via single-atom alloying, Nat. Nanotechnol. 16 (12) (2021) 1386–1393, https://doi.org/10.1038/s41565-021-00974-5.

[32] H.A. Hansen, C. Shi, A.C. Lausche, A.A. Peterson, J.K. Nørskov, Bifunctional alloys for the electroreduction of CO_2 and CO, Phys. Chem. Chem. Phys. 18 (13) (2016) 9194–9201, https://doi.org/10.1039/c5cp07717f.

[33] T. Sun, J. Wu, X. Lu, X. Tang, Selectivities of stepped Cu–M (M = Pt, Ni, Pd, Zn, Ag, Au) bimetallic surface environment for C_1 and C_2 Pathways, Langmuir 40 (17) (2024) 9289–9298, https://doi.org/10.1021/acs.langmuir.4c00843.

[34] C. An, Y. Shen, W. Yan, L. Dai, C. An, Surface-tuning nanoporous $AuCu_3$ engineering syngas proportion by electrochemical conversion of CO_2, Nano Res 14 (11) (2021) 3907–3912, https://doi.org/10.1007/s12274-021-3313-3.

[35] D. Shu, M. Wang, F. Tian, H. Zhang, C. Peng, A dual-cathode study on Ag-Cu sequential CO_2 electroreduction towards hydrocarbons, *J. CO_2 Util.* 45 (2021) 101444, https://doi.org/10.1016/j.jcou.2021.101444.

[36] P. Wang, H. Yang, Y. Xu, X. Huang, J. Wang, M. Zhong, et al., Synergized Cu/Pb core/shell electrocatalyst for high-efficiency CO_2 reduction to C_{2+} Liquids, ACS Nano 15 (1) (2021) 1039–1047, https://doi.org/10.1021/acsnano.0c07869.

[37] K. Ye, A. Cao, J. Shao, G. Wang, R. Si, N. Ta, et al., Synergy effects on Sn-Cu alloy catalyst for efficient CO_2 electroreduction to formate with high mass activity, Sci. Bull. (Beijing) 65 (9) (2020) 711–719, https://doi.org/10.1016/j.scib.2020.01.020.

[38] S. Ma, M. Sadakiyo, M. Heima, R. Luo, R.T. Haasch, J.I. Gold, et al., Electroreduction of carbon dioxide to hydrocarbons using bimetallic Cu-Pd catalysts with different mixing patterns, J. Am. Chem. Soc. 139 (1) (2017) 47–50, https://doi.org/10.1021/jacs.6b10740.

[39] A.E. Green, J. Justen, W. Schöllkopf, A.S. Gentleman, A. Fielicke, S.R. Mackenzie, IR signature of size-selective CO_2 activation on small platinum cluster anions, Pt n-(n=4-7), Angew. Chem. 130 (45) (2018) 15038–15042, https://doi.org/10.1002/ange.201809099.

[40] L. Ou, W. Long, J. Huang, Y. Chen, J. Jin, Theoretical insight into effect of doping of transition metal M (M = Ni, Pd and Pt) on CO_2 reduction pathways on Cu(111) and understanding of origin of electrocatalytic activity, RSC Adv. 7 (20) (2017) 11938–11950, https://doi.org/10.1039/c6ra28815d.

[41] X. Gao, Y. Zhang, M. Wang, L. Liu, J. Li, Z. Li, et al., Improving the CO_2 hydrogenation activity of photocatalysts via the synergy between surface frustrated lewis pairs and the CuPt alloy, ACS Sustain Chem. Eng. 11 (14) (2023) 5597–5607, https://doi.org/10.1021/acssuschemeng.2c07626.

[42] H.P. Yang, Q. Lin, H.W. Zhang, Y. Wu, L.D. Fan, X.Y. Chai, et al., Selective electrochemical reduction of CO_2 by a binder-free platinum/nitrogen-doped carbon nanofiber/copper foil catalyst with remarkable efficiency and reusability, Electrochem Commun. 93 (2018) 138–142, https://doi.org/10.1016/j.elecom.2018.06.018.

[43] M. Chhetri, M. Wan, Z. Jin, J. Yeager, C. Sandor, C. Rapp, et al., Dual-site catalysts featuring platinum-group-metal atoms on copper shapes boost hydrocarbon formations in electrocatalytic CO_2 reduction", Nat. Commun. 14 (2023) 3075, https://doi.org/10.1038/s41467-023-38777-y.

[44] X. Guo, Y. Zhang, C. Deng, X. Li, Y. Xue, Y.-M. Yan, et al., Composition dependent activity of Cu-Pt nanocrystals for electrochemical reduction of CO_2, Chem. Commun. 51 (7) (2015) 1345–1348, https://doi.org/10.1039/C4CC08175G.

[45] X. Zhao, B. Luo, R. Long, C. Wang, Y. Xiong, Composition-dependent activity of Cu-Pt alloy nanocubes for electrocatalytic CO_2 reduction, J. Mater. Chem. A Mater. 3 (8) (2015) 4134–4138, https://doi.org/10.1039/c4ta06608a.

[46] A. Sarkar, A. Manthiram, Synthesis of Pt@Cu Core-shell nanoparticles by galvanic displacement of Cu by Pt^{4+} ions and their application as electrocatalysts for oxygen reduction reaction in fuel cells, J. Phys. Chem. C. 114 (10) (2010) 4725–4732, https://doi.org/10.1021/jp908933r.

[47] M.C. Biesinger, Advanced analysis of copper X-ray photoelectron spectra, Surf. Interface Anal. 49 (13) (2017) 1325–1334, https://doi.org/10.1002/sia.6239.

[48] I. Khalakhan, M. Vorokhta, X. Xie, L. Piliai, I. Matolínová, On the interpretation of X-ray photoelectron spectra of Pt-Cu bimetallic alloys, J. Electron Spectrosc. Relat. Phenom. 246 (147027) (2021) 1–9, https://doi.org/10.1016/j.elspec.2020.147027.

[49] Y. Li, L. Guo, M. Du, C. Tian, G. Zhao, Z. Liu, Z. Liang, K. Hou, J. Chen, X. Liu, L. Jiang, B. Nan, L. Li, Unraveling distinct effects between CuO_X and PtCu alloy sites in Pt−Cu bimetallic catalysts for CO oxidation at different temperatures, Nat. Commun. 15 (5598) (2024) 1–10, https://doi.org/10.1038/s41467-024-49968-6.

[50] F. Yu, W. Zhou, Alloying and dealloying of CuPt bimetallic nanocrystals, Prog. Nat. Sci.: Mater. Int. 23 (3) (2013) 331–337, https://doi.org/10.1016/j.pnsc.2013.04.009.

[51] S. Khanal, A. Spitale, N. Bhattarai, D. Bahena, J.J. Velazquez-Salazar, S. Mejía-Rosales, M. M. Mariscal, M. José-Yacaman, Synthesis, characterization, and growth simulations of Cu–Pt bimetallic nanoclusters, Beilstein J. Nanotechnol. 5 (2014) 1371–1379, https://doi.org/10.3762/bjnano.5.150.

[52] J.F. Moulder, W.F. Stickle, P.E. Sobol, and K.D. Bomben, Handbook of X-ray Photoelectron Spectroscopy: A Reference Book of Standard Spectra for Identification and Interpretation of XPS Data, Perkin-Elmer Corporation, Physical Electronics Division, Eden Prairie, Minnesota, 1992.

[53] J. Maya-Cornejo, R. Carrera-Cerritos, D. Sebastián, J. Ledesma-García, L. G. Arriaga, A.S. Aricó, et al., PtCu catalyst for the electro-oxidation of ethanol in an alkaline direct alcohol fuel cell, Int J. Hydrog. Energy 42 (46) (2017) 27919–27928, https://doi.org/10.1016/j.ijhydene.2017.07.226.

[54] S. Pérez-Rodríguez, E. Pastor, M.J. Lázaro, Noble metal-free catalysts supported on carbon for CO_2 electrochemical reduction, J. CO_2 Util. 18 (2017) 41–52, https://doi.org/10.1016/j.jcou.2017.01.010.

[55] A. Wadas, I.A. Rutkowska, M. Bartel, S. Zoladek, K. Rajeshwar, P.J. Kulesza, Rotating ring-disk voltammetry: diagnosis of catalytic activity of metallic copper catalysts toward CO_2 electroreduction, Russ. J. Electrochem. 53 (10) (2017) 1194–1203, https://doi.org/10.1134/S1023193517100135.

[56] B. Beden, A. Bewick, M. Razaq, J. Weber, On the nature of reduced CO_2 an IR spectroscopic investigation, J. Electroanal. Chem. 139 (1) (1982) 203–206, https://doi.org/10.1016/0022-0728(82)85116-4.

[57] S. Pérez-Rodríguez, N. Rillo, M.J. Lázaro, E. Pastor, Pd catalysts supported onto nanostructured carbon materials for CO_2 valorization by electrochemical reduction, Appl. Catal. B 163 (2015) 83–95, https://doi.org/10.1016/j.apcatb.2014.07.031.

[58] A. López-Cudero, A. Cuesta, C. Gutiérrez, Potential dependence of the saturation CO coverage of Pt electrodes: the origin of the pre-peak in CO-stripping voltammograms. Part 1: Pt(111), J. Electroanal. Chem. 579 (1) (2005) 1–12, https://doi.org/10.1016/j.jelechem.2005.01.018.

[59] D. Ewis, M. Arsalan, M. Khaled, D. Pant, M.M. Ba-Abbad, A. Amhamed, et al., Electrochemical reduction of CO_2 into formate/formic acid: a review of cell design and operation, Sep. Purif. Technol. 316 (2023) 123811, https://doi.org/10.1016/j.seppur.2023.123811.

[60] D. Raciti, C. Wang, Recent advances in CO_2 reduction electrocatalysis on copper, ACS Energy Lett. 3 (7) (2018) 1545–1556, https://doi.org/10.1021/acsenergylett.8b00553.

[61] T.W. Jiang, K. Jiang, W.-B. Cai, Electrochemical CO_2 reduction on Pd-based electrodes: from mechanism understanding to rational catalyst design, J. Mater. Chem. A 12 (2024) 21515–21530, https://doi.org/10.1039/d4ta02379j.

[62] E. Morallón, J.L. Vázquez, J.M. Pérez, Electrochemical behaviour of Pt (100), Pt (111) and Pt polycrystalline surfaces in hydrogencarbonate solution, J. Electroanal. Chem. 380 (1-2) (1995) 47–53, https://doi.org/10.1016/0022-0728(94)03615-7.

[63] G. Marcandalli, M.C.O. Monteiro, A. Goyal, M.T.M. Koper, Electrolyte effects on CO_2 electrochemical reduction to CO, Acc. Chem. Res 55 (14) (2022) 1900–1911, https://doi.org/10.1021/acs.accounts.2c00080.

[64] J.T. Song, H. Song, B. Kim, J. Oh, Towards higher rate electrochemical CO_2 conversion: From liquid-phase to gas-phase systems, Catalysts 9 (3) (2019) 224, https://doi.org/10.3390/catal9030224.

[65] F.P. García de Arquer, C.T. Dinh, A. Ozden, J. Wicks, C. McCallum, A.R. Kirmani, et al., CO_2 electrolysis to multicarbon products at activities greater than 1 A cm^{-2}, Science 367 (6478) (2020) 661–666, https://doi.org/10.1126/science.aay4217.

[66] M. Quentmeier, B. Schmid, H. Tempel, R.A. Eichel, Modular CO_2-to-CO electrolysis short-stack design-impact of temperature gradients and insights into position-dependent cell behavior, ACS Sustain Chem. Eng. 12 (9) (2024) 3876–3885, https://doi.org/10.1021/acssuschemeng.4c00630.

[67] X. Meng, G. Pan, H. Liu, Y. Qian, X. Wang, C. Wang, L. Hu, H. Wang, Q. Chen, Ultrasmall Cu nanocrystals dispersed in nitrogen-doped carbon as highly efficient catalysts for CO_2 electroreduction, ACS Appl. Mater. Interfaces 14 (15) (2022) 17240–17248, https://doi.org/10.1021/acsami.2c00050.

[68] H. Guzmán, J. Albo, A. Irabien, M. Castellino, S. Hernández, Role of electrochemical cell configuration on the selectivity of CuZnAl-oxide-based electrodes for the continuous CO_2 conversion: aqueous electrolyte vs. catholyte-less configuration, Discov. Chem. Eng. 4 (2024) 12, https://doi.org/10.1007/s43938-024-00049-6.

[69] X. Zheng, P. De Luna, F.Pelayo García de Arquer, B. Zhang, N. Becknell, M.B. Ross, et al., Sulfur-modulated tin sites enable highly selective electrochemical reduction of CO_2 to Formate, Joule 1 (4) (2017) 794–805, https://doi.org/10.1016/j.joule.2017.09.014.

[70] S. Kim, W.J. Dong, S. Gim, W. Sohn, J.Y. Park, C.J. Yoo, et al., Shape-controlled bismuth nanoflakes as highly selective catalysts for electrochemical carbon dioxide reduction to formate, Nano Energy 39 (2017) 44–52, https://doi.org/10.1016/j.nanoen.2017.05.065.
[71] M. Zoli, D. Roldán, H. Guzmán, M. Castellino, A. Chiodoni, K. Bejtka, et al., Facile and scalable synthesis of Cu_2O-SnO_2 catalyst for the photoelectrochemical CO_2 conversion, Catal. Today 413-415 (2023) 113985, https://doi.org/10.1016/j.cattod.2022.12.016.
[72] J. Sirijaraensre, J. Limtrakul, Hydrogenation of CO_2 to formic acid over a Cu-embedded graphene: a DFT study, Appl. Surf. Sci. 364 (2016) 241–248, https://doi.org/10.1016/j.apsusc.2015.12.117.
[73] M.D. Esrafili, F. Sharifi, L. Dinparast, Catalytic hydrogenation of CO_2 over Pt- and Ni-doped graphene: a comparative DFT study, J. Mol. Graph Model 77 (2017) 143–152, https://doi.org/10.1016/j.jmgm.2017.08.016.
[74] N.E. Şahin, C. Comminges, S. Arrii, T.W. Napporn, K.B. Kokoh, CO_2-to-HCOOH electrochemical conversion on nanostructured Cu_xPd_{100-x}/carbon catalysts, ChemElectroChem 8 (7) (2021) 1362–1368, https://doi.org/10.1002/celc.202100268.
[75] R. Kortlever, I. Peters, S. Koper, M.T.M. Koper, Electrochemical CO_2 reduction to formic acid at low overpotential and with high faradaic efficiency on carbon-supported bimetallic Pd-Pt nanoparticles, ACS Catal. 5 (7) (2015) 3916–3923, https://doi.org/10.1021/acscatal.5b00602.
[76] C. Ye, F. Dattila, X. Chen, N. López, M.T.M. Koper, Influence of cations on HCOOH and CO formation during CO_2 reduction on a $Pd_{ML}Pt(111)$ electrode, J. Am. Chem. Soc. 145 (36) (2023) 19601–19610, https://doi.org/10.1021/jacs.3c03786.
[77] K. Gupta, M. Bersani, J.A. Darr, Highly efficient electro-reduction of CO_2 to formic acid by nano-copper, J. Mater. Chem. A Mater. 4 (36) (2016) 13786–13794, https://doi.org/10.1039/c6ta04874a.
[78] W.J. Durand, A.A. Peterson, F. Studt, F. Abild-Pedersen, J.K. Nørskov, Structure effects on the energetics of the electrochemical reduction of CO_2 by copper surfaces, Surf. Sci. 605 (15–16) (2011) 1354–1359, https://doi.org/10.1016/j.susc.2011.04.028.
[79] T. Cheng, H. Xiao, W.A. Goddard, Reaction mechanisms for the electrochemical reduction of CO_2 to CO and formate on the Cu(100) surface at 298 K from quantum mechanics free energy calculations with explicit water, J. Am. Chem. Soc. 138 (42) (2016) 13802–13805, https://doi.org/10.1021/jacs.6b08534.
[80] A. Bagger, W. Ju, A.S. Varela, P. Strasser, J. Rossmeisl, Electrochemical CO_2 reduction: a classification problem, ChemPhysChem 18 (2017) 3266–3273, https://doi.org/10.1002/cphc.201700736.
[81] D. Giusi, M. Miceli, C. Genovese, G. Centi, S. Perathoner, C. Ampelli, et al., In situ electrochemical characterization of Cu_XO-based gas-diffusion electrodes (GDEs) for CO_2 electrocatalytic reduction in presence and absence of liquid electrolyte and relationship with C_{2+} products formation, Appl. Catal. B: Environ. 318 (2022) 121845, https://doi.org/10.1016/j.apcatb.2022.121845.
[82] R.M. Arán-Ais, F. Scholten, S. Kunze, R. Rizo, B. Roldan Cuenya, et al., "The role of in situ generated morphological motifs and Cu(i) species in C_{2+} product selectivity during CO_2 pulsed electroreduction", Nat. Energy 5 (2020) 317–324, https://doi.org/10.1038/s41560-020-059-9.
[83] S. Wang, T. Kou, S.E. Baker, E.B. Duoss, Y. Li, Recent progress in electrochemical reduction of CO_2 by oxide-derived copper catalysts, Mater. Today Nano 12 (2020) 100096, https://doi.org/10.1016/j.mtnano.2020.100096.
[84] L. Mandal, K.R. Yang, M.R. Motapothula, D. Ren, P. Lobaccaro, A. Patra, M. Sherburne, V.S. Batista, B.S. Yeo, J.W. Ager, J. Martin, T. Venkatesan, Investigating the role of copper oxide in electrochemical CO_2 reduction in real time, ACS Appl. Mater. Interfaces 10 (10) (2018) 8574–8584, https://doi.org/10.1021/acsami.7b15418.
[85] D. Gao, R.M. Arán-Ais, H.S. Jeon, B. Roldan Cuenya, Rational catalyst and electrolyte design for CO_2 electroreduction towards multicarbon products, Nat. Catal. 2 (3) (2019) 198–210, https://doi.org/10.1038/s41929-019-0235-5.
[86] J.-J. Velasco-Veléz, T. Jones, D. Gao, E. Carbonio, R. Arrigo, C.-J. Hsu, et al., The role of the copper oxidation state in the electrocatalytic reduction of CO_2 into valuable hydrocarbons, ACS Sustain. Chem. Eng. 7 (2) (2019) 1485–1492, https://doi.org/10.1021/acssuschemeng.8b05106.
[87] J.E. Pander III, D. Ren, Y. Huang, N.W.X. Loo, S.H.L. Hong, B.S. Yeo, Understanding the heterogeneous electrocatalytic reduction of carbon dioxide on oxide-derived catalysts, ChemElectroChem 5 (2) (2018) 219–237, https://doi.org/10.1002/celc.201701100.
[88] S. Wang, T. Kou, J.B. Varley, S.A. Akhade, S.E. Weitzner, S.E. Baker, et al., Cu_2O/CuS nanocomposites show excellent selectivity and stability for formate generation via electrochemical reduction of carbon dioxide, ACS Mater. Lett. 3 (1) (2021) 100–109, https://doi.org/10.1021/acsmaterialslett.0c00520.
[89] F. Yang, T. Yang, J. Li, P. Li, Q. Zhang, H. Lin, et al., Boosting the electroreduction of CO_2 to liquid products via nanostructure engineering of Cu_2O catalysts, J. Catal. 432 (2024) 115458, https://doi.org/10.1016/j.jcat.2024.115458.
[90] D. Li, L. Huang, T. Liu, J. Liu, L. Zhen, J. Wu, Electrochemical reduction of carbon dioxide to formate via nano-prism assembled CuO microspheres, Chemosphere 237 (2019) 124527, https://doi.org/10.1016/j.chemosphere.2019.124527.
[91] M. Fan, C. Ma, T. Lei, J. Jung, D. Guay, J. Qiao, Aqueous-phase electrochemical reduction of CO_2 based on SnO_2-CuO nanocomposites with improved catalytic activity and selectivity, Catal. Today 318 (2018) 2–9, https://doi.org/10.1016/j.cattod.2017.09.018.
[92] S.H. Lee, J.C. Lin, M. Farmand, A.T. Landers, J.T. Feaster, J.E.Avilés Acosta, et al., Oxidation state and surface reconstruction of Cu under CO_2 reduction conditions from in situ X-ray characterization, J. Am. Chem. Soc. 143 (2021) 588–592, https://doi.org/10.1021/jacs.0c10017.
[93] F. Hu, X. Xu, Y. Sun, C. Hu, S. Shen, Y. Wang, et al., Reaction pathway regulation for gaseous and liquid products of electrocatalytic CO_2 reduction under adsorbate interactions, Angew. Chem. Int. Ed. 64 (2025) e202419456, https://doi.org/10.1002/anie.202419456.
[94] R. Reske, M. Duca, M. Oezaslan, K.J.P. Schouten, M.T.M. Koper, P. Strasser, Controlling catalytic selectivities during CO_2 electroreduction on thin Cu metal overlayers, J. Phys. Chem. Lett. 4 (2013) 2410–2413, https://doi.org/10.1021/jz401087q.
[95] T. Hou, J. Zhu, H. Gu, X. Li, Y. Sun, Z. Hua, R. Shao, C. Chen, B. Hu, L. Mai, S. Chen, D. Wang, J. Zhang, Switching CO_2 electroreduction toward C_{2+} products and CH_4 by regulating the dimerization and protonation in platinum/copper catalysts (vol), Angew. Chem. Int. Ed. 2025 (2025) e202424749, https://doi.org/10.1002/anie.202424749.